Palaeogeography, Palaeoclimatology, Palaeoecology 571 (2021) 109990

Contents lists available at ScienceDirect

Palaeogeography, Palaeoclimatology, Palaeoecology

journal homepage: www.elsevier.com/locate/palaeo

Chronostratigraphy and age modeling of Pleistocene drill cores from the Olduvai Basin, Tanzania (Olduvai Gorge Coring Project)

Alan L. Deino [a,*], Clifford Heil Jr [b], John King [b], Lindsay J. McHenry [c], Ian G. Stanistreet [d,e], Harald Stollhofen [f], Jackson K. Njau [e,g], Joshua Mwankunda [h], Kathy D. Schick [e,i], Nicholas Toth [e,i]

[a] Berkeley Geochronology Center, 2455 Ridge Rd., Berkeley, CA 94709, USA
[b] Graduate School of Oceanography, South Ferry Road, Narragansett, RI 02882, USA
[c] Department of Geosciences, University of Wisconsin-Milwaukee, 3209 N. Maryland Ave., Milwaukee, WI 53211, USA
[d] Dept. Earth, Ocean and Ecological Sciences, University of Liverpool, Brownlow Street, Liverpool L69 3GP, UK
[e] The Stone Age Institute, Bloomington, IN 47407-5097, USA
[f] GeoZentrum Nordbayern, Friedrich-Alexander-University (FAU) Erlangen-Nürnberg, Schloßgarten 5, 91054 Erlangen, Germany
[g] Department of Earth and Atmospheric Sciences, Indiana University, 1001 East 10th Street, Bloomington, IN 47405-1405, USA
[h] Ngorongoro Conservation Area Authority, P.O. Box 1, Ngorongoro Crater, Arusha, Tanzania
[i] Department of Anthropology, Indiana University, 702 E Kirkwood Ave., Bloomington, IN 47405-1405, USA.

ARTICLE INFO

Keywords:
$^{40}Ar/^{39}Ar$ dating
Magnetostratigraphy
Tephrostratigraphy
Bayesian
East Africa

ABSTRACT

The Olduvai Gorge Coring Project drilled a total of 611.72 m of core (575.48 m recovered) of mostly fluvio-lacustrine and fan-delta volcaniclastic Pleistocene strata at three sites in the Olduvai Basin, Tanzania, in 2014. We have developed a chronostratigraphic framework for three of the cores based on $^{40}Ar/^{39}Ar$ dating of core and outcrop volcanic and volcaniclastic units, core paleomagnetic stratigraphy, and tephrochemical correlation between cores and from core to outcrop. This framework is then used to constrain Bayesian stratigraphic age models which permit age estimates for desired core levels with realistic confidence intervals. The age models reveal that the deepest core level reached at 245 mbs is ~2.24 Ma, ~210 kyr older than the oldest strata exposed at Olduvai Gorge. Strata net accretion rates in this early phase of basin history were relatively rapid (57–69 cm/kyr), but decreased within ~250 kyr to ~15 cm/kyr in Lower Bed I. Rates rebounded partially in Upper Bed I, but subsequently declined to <10 cm/kyr by Middle to Upper Pleistocene. The age models also provide new estimates for the basal contacts of upper Olduvai Gorge stratigraphic units that have been previously difficult to calibrate: Bed III at 1.14 ± 0.05 (95% confidence interval), Bed IV at 0.93 ± 0.08, Masek at 0.82 ± 0.06, and Ndutu at 0.50 ± 0.04 Ma. Finally, based on recently acquired seismic imaging identifying basement another 135 m beneath the bottom of the deepest core, extrapolation of net accretion rates suggests that sedimentation began at this site in the Olduvai Basin at ~2.5 Ma.

1. Introduction

The Olduvai Gorge Coring Project (OGCP) was initiated in 2014 to investigate the stratigraphy and paleoclimate of the Olduvai Basin, Tanzania, through recovery of deep drill cores into the basinal depocenter near sites of paleoanthropological interest. The project is staffed by an international, multidisciplinary consortium of anthropologists and earth scientists, under the leadership of Drs. Nicholas Toth, Kathy Schick, Jackson Njau and Ian Stanistreet. A total of 575.48 m of 6 cm core was recovered from four holes (77.16, 236.55, 121.19, and 146.9 m from cores 1A (lat. 2.9860°S, long. 35.3428°E), 2A (lat. 2.9786°S, long. 35.32375°E), 3A, and 3B (lat. 2.944867°S, long. 35.380967°E), respectively) (Fig. 1).

The fossils and artifacts of Olduvai Gorge are world renowned. Paleontological interest in the area was initiated in 1913 with the discovery of a prehistoric human skeleton (OH 1) in the Main Gorge (Reck,

* Corresponding author.
E-mail addresses: adeino@bgc.org (A.L. Deino), chiph@uri.edu (C. Heil), jwking@uri.edu (J. King), lmchenry@uwm.edu (L.J. McHenry), harald.stollhofen@fau.de (H. Stollhofen), jknjau@indiana.edu (J.K. Njau), joshua.mwankunda@ncaa.go.tz (J. Mwankunda), toth@indiana.edu (K.D. Schick), kaschick@indiana.edu (N. Toth).

https://doi.org/10.1016/j.palaeo.2020.109990
Received 18 June 2020; Received in revised form 19 August 2020; Accepted 20 August 2020
Available online 22 October 2020

1914), with excavations beginning in 1931 under the direction of Louis and Mary Leakey. In parallel with the continuing paleontological and archeological interest in this region, the geological setting has been intensively investigated and is reasonably well understood; the seminal work on the geologic history and stratigraphy of the Olduvai Basin is Hay (1976), while Stollhofen and Stanistreet (2012) undertook a structural re-evaluation of basin evolution. Stratigraphy of the gorge and surrounding regions are complex, however, and many subsequent studies have contributed to our understanding of the geologic record, and particularly, given the context of this research, to the chronostratigraphy through application of radiometric dating (Evernden and Curtis, 1965; Curtis and Hay, 1972; Hay, 1992; Walter et al., 1991; Manega, 1994; Blumenschine et al., 2003; Deino, 2012; Dominguez-Rodrigo et al., 2013; Diez-Martin et al., 2015), magnetostratigraphy (Grommé and Hay, 1963, 1967, 1971; Grommé et al., 1970; Hay, 1976; Tamrat et al., 1995), and tephrostratigraphy (McHenry, 2005; McHenry et al., 2008; Stollhofen et al., 2008; McHenry, 2012; McHenry et al., 2016; Habermann et al., 2016; McHenry and Stanistreet, 2018).

Olduvai Gorge is an east-northeast to west-southwest Upper Pleistocene to Holocene fluvial incision into Pleistocene sedimentary and volcanic rocks (Fig. 1). These beds were deposited in an enclosed saline-alkaline lake basin westward of major faults of the eastern branch of the East African Rift and volcanoes of the Ngorongoro Volcanic Highlands (NVH) in northern Tanzania (Hay, 1976; Hay and Kyser, 2001). The basin is underlain by metamorphic rocks of the Archean Tanzanian Craton and the late Proterozoic Pan-African Mozambique Belt, unconformably overlain by a series of fluviolacustrine deposits and intercalated lavas, ignimbrites, fallout tuffs, and volcaniclastic sediments. The oldest exposed strata in the basin are ~2.0 Ma ignimbrites sourced from Ngorongoro Caldera in the NVH.

The stratigraphic nomenclature of the exposed Pleistocene basin-fill deposits was established by Hay (1976) after Reck (1914, 1951), with modifications by McHenry (2012), Habermann et al. (2016), McHenry and Stanistreet et al. (2018), Stanistreet et al. (2018) and Stanistreet et al. (2020a). As well as lithostratigraphy, the latter authors introduce a sequence stratigraphic approach, whereby basinwide erosion surfaces, caused by lake-level falls, can be used as time-correlative surfaces. This was an approach that was used intuitively by Hay (1976) in his definition of most boundaries (Bed II/Bed III; Bed III/Bed IV; Bed IV/Masek; Masek/Ndutu), all based upon major disconformities. Such boundaries are used in the correlative figures drawn in this manuscript. According to Hay (1976), the oldest strata above a basal welded pyroclastic flow (Naabi Ignimbrite) was divided into Bed I (up through Tuff IF, ~2.0–1.8 Ma; Deino, 2012), and younger units whose precise ages are under study (Beds II, III, IV, Masek, and Ndutu). Current nomenclature incorporates the CFCT and Naabi Ignimbrite into the underlying Ngorongoro Formation (Stanistreet et al., 2020a).

Here we present stratigraphic age models for three of the OGCP cores. Our procedure for building these models is firstly to date core tuffs and lavas by the $^{40}Ar/^{39}Ar$ method, secondly to use tephrochemical correlation to tie new and previously published outcrop radiometric ages into the cores, and thirdly to delineate a paleomagnetic reversal stratigraphy directly from core material. We then use the resulting chronostratigraphic framework as input to Bayesian stratigraphic age modelling, which yields estimates of absolute ages and realistic uncertainties for all covered depths at 20 cm resolution.

2. Methods

2.1. Core depth scales

Core depth scales were generated using the drilling and core metadata, and are equivalent to the IODP CSF-B depth scale (IODP-MI, 2011; Arculus et al., 2015). Depths indicate distance from the ground surface to the location within the recovered core, applying a linear compression scaling algorithm if recovery for a core is above 100%. The drilling and core metadata are publicly available at dx.doi.org/10.17605/OSF.IO/3SKMA.

2.2. $^{40}Ar/^{39}Ar$ dating

We report here $^{40}Ar/^{39}Ar$ dating for OGCP core tuff layers, a trachyte lava, and a basalt to trachybasaltic lava flow (Habermann et al., 2016; Stanistreet et al., 2020b), as well as seven new ages from outcrop exposures of tuffs that are relevant to development of the core chronostratigraphy. The dating methodology employed here has been described previously (Deino, 2012), thus our discussion will concentrate on the core processing and data reduction protocol.

All OGCP cores were logged at 1 cm accuracy, as summarized by Stanistreet et al., 2020a. Their stratigraphic nomenclature is adopted here as well. Tuffaceous zones in the OGCP cores were identified megascopically and by smear-slide examination immediately after core splitting during the Initial Core Description at the National Lacustrine Core Facility (LacCore) at the University of Minnesota (Twin Cities). Samples ($n = 73$) were processed for $^{40}Ar/^{39}Ar$ dating at the Berkeley Geochronology Center (BGC); of these, 61 yielded viable mineral separates that were irradiated and dated. In addition, three samples of a basalt to trachybasaltic lava were sampled at the base, interior, and top of the flow for dating purposes.

Sample processing of tuff consisted of gentle hand-crushing in a ceramic mortar, wet-rinsing in distilled water through a new 90- or 400-μm sieve bag, drying, and examination of the mineralogical characteristics of the coarser fraction under a binocular microscope. A trachyte lava from the base of Core 3A, containing K-feldspar phenocrysts, was comminuted by hand crushing in a metal mortar. Feldspars were concentrated with a Frantz magnetic separator (if necessary), hand-picked, washed in 5% HF and distilled water, and hand-picked again to obtain the clearest, most inclusion-free material.

Sample processing for the basalt to trachybasaltic Bed I lava flow consisted of hand-crushing in a metallic mortar, sieving to 40–60 mesh (250–400 μm), removal of highly magnetic and weakly magnetic fractions with a Frantz isodynamic separator, hand-picking to remove phenocrysts and altered material, and ultrasonic baths in distilled water.

The mineral and rock separates were irradiated in the Cd-lined CLICIT position of the Oregon State University TRIGA reactor in 11 batches (Table S1). Sanidine from the Fish Canyon Tuff of Colorado served as an irradiation fluence monitor mineral for three irradiations (orbitally referenced age of 28.201 ± 0.023 1σ Ma; Kuiper et al., 2008), whereas all other irradiations used sanidine phenocrysts from the Alder Creek Rhyolite of California (orbitally referenced age = 1.1848 ± 0.0006 Ma (Niespolo et al., 2017). Reactor-induced isotopic production ratios for these irradiations were: $(^{36}Ar/^{37}Ar)_{Ca} = 2.65 \pm 0.02 \times 10^{-4}$, $(^{38}Ar/^{37}Ar)_{Ca} = 1.96 \pm 0.08 \times 10^{-5}$, $(^{39}Ar/^{37}Ar)_{Ca} = 6.95 \pm 0.09 \times 10^{-4}$, $(^{37}Ar/^{39}Ar)_{K} = 2.24 \pm 0.16 \times 10^{-4}$, $(^{38}Ar/^{39}Ar)_{K} = 1.220 \pm 0.003 \times 10^{-2}$, $(^{40}Ar/^{39}Ar)_{K} = 2.5 \pm 0.9 \times 10^{-4}$. Atmospheric $^{40}Ar/^{36}Ar = 298.56 \pm 0.31$ (Lee et al., 2006) and decay constants follow Min et al. (2000). Previously published $^{40}Ar/^{39}Ar$ ages referenced herein (Deino et al., 2006) are recalculated for consistency using the decay constants and Fish Canyon sanidine age stated above.

Following a period of at least several weeks of radiological 'cooling' after irradiation, the feldspars were analyzed individually by the $^{40}Ar/^{39}Ar$ technique using single-crystal incremental heating (SCIH). Here, individual phenocrysts are incrementally heated and measured for argon isotopes on a noble-gas mass spectrometer in 3–9 steps (depending on grain size and gas yield) at progressively increasing power to fusion. The matrix material from the alkaline flow was analyzed as a small bulk analysis (weight ~ 10–20 mg), also by the incremental heating technique (4–8 steps). Isotope measurements were conducted on a Nu Instruments *Noblesse* noble-gas mass spectrometer employing simultaneous multi-isotope measurement on ion-counting electron multiplier detectors (Deino et al., 2019a, 2019b).

The incremental release experiments are examined for intervals of

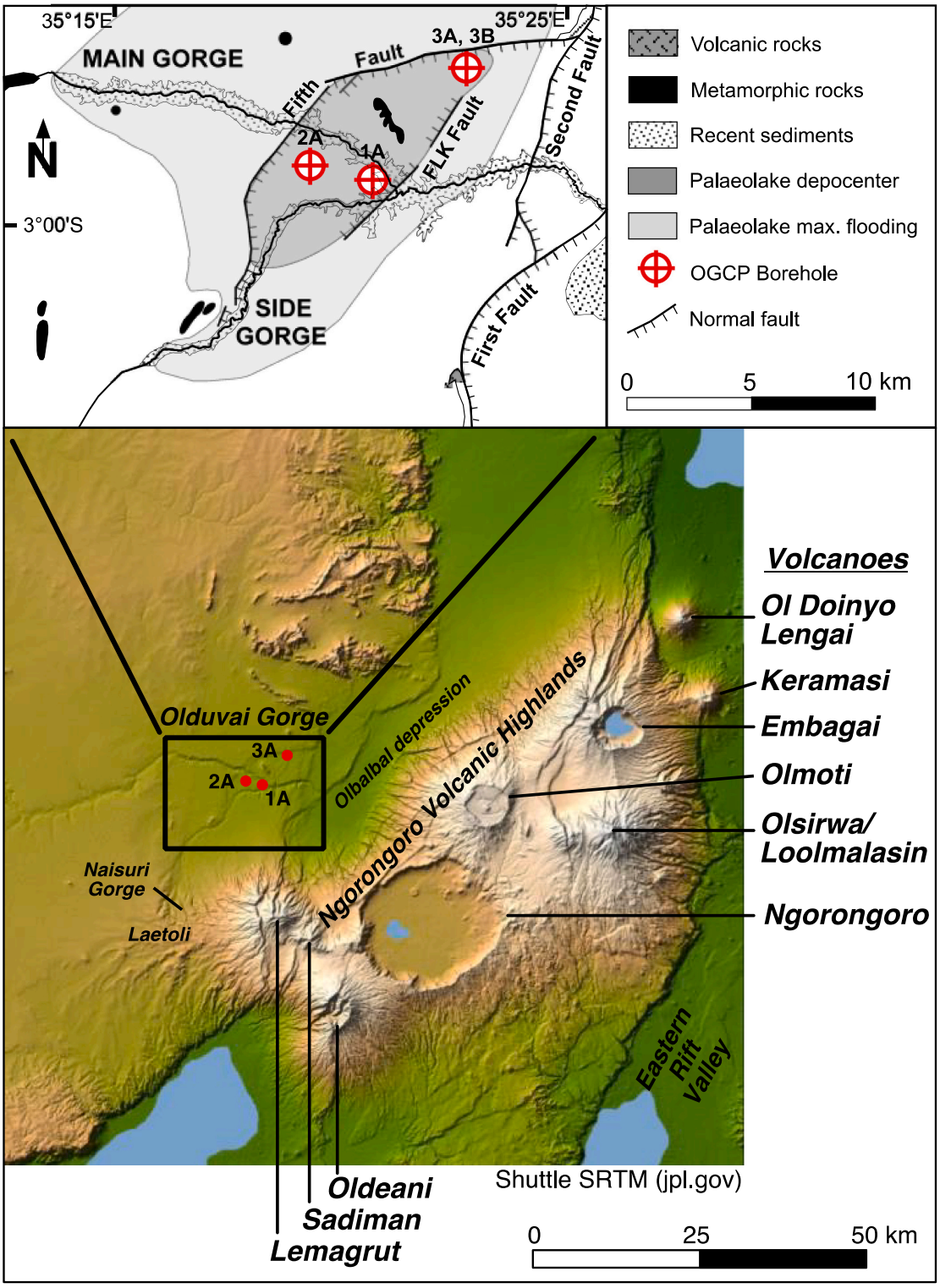

Fig. 1. Location map and setting of the OGCP in northern Tanzania.

calculated age consistency as a fraction of ^{39}Ar released. The 'plateau' algorithm follows Fleck et al., (1977), but uses an acceptable MSWD as a statistical criterion ('mean squared weighted deviation'), with a threshold probability >95% that the observed scatter is caused by analytical error alone and that geological scatter is not demonstrated.

As found previously at Olduvai Gorge and elsewhere in East Africa (e.g., Deino, 2012; Deino et al., 2018; Deino et al., 2019a, 2019b), anomalously old single-crystal ^{40}Ar/^{39}Ar age outliers are fairly common in tuffaceous samples, and derive from a variety of sources. These include antecrysts acquired shortly before or during eruption and incompletely outgassed, excess ^{40}Ar trapped in primary phenocrysts likewise incompletely outgassed, xenocrysts plucked from a volcano's surface during eruption or acquired during fluvial transport, and incipient alteration of feldspars (particularly their glass inclusions). The

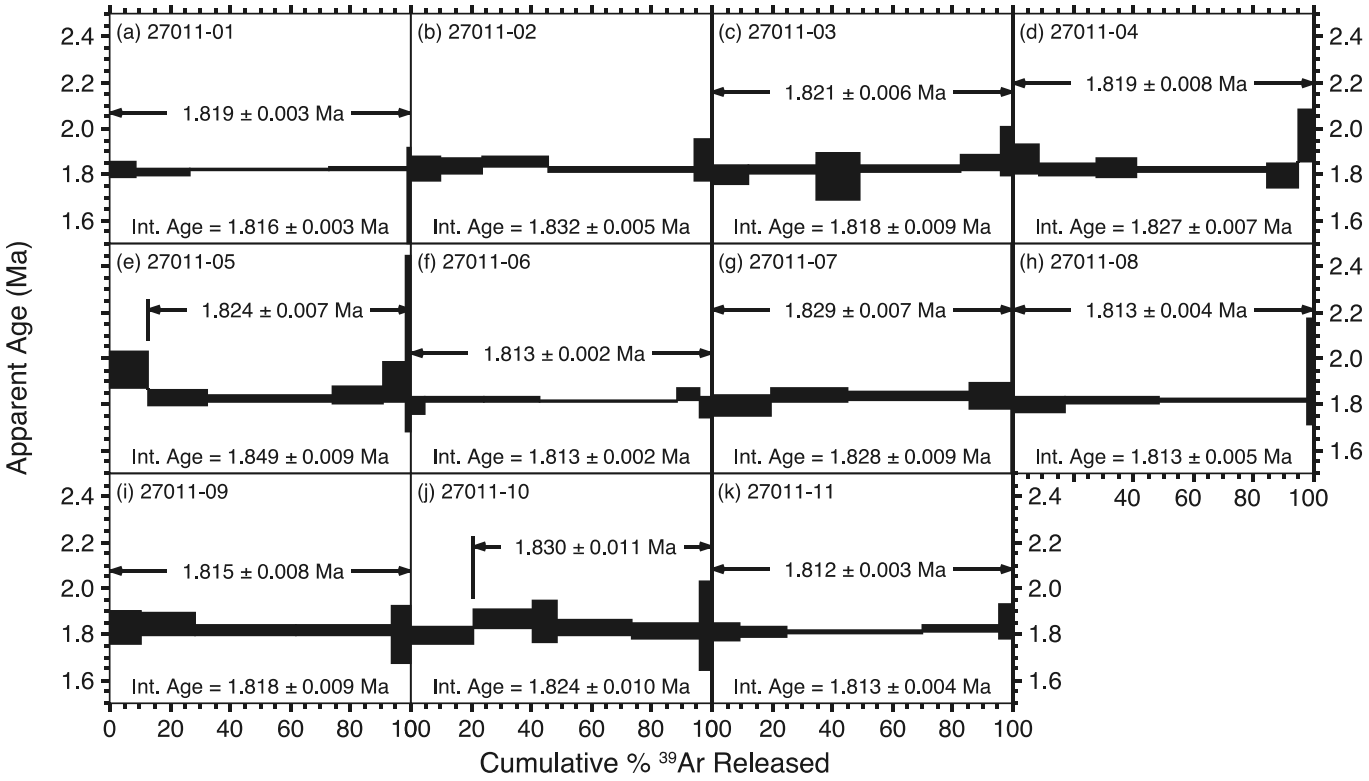

Fig. 2. Representative $^{40}Ar/^{39}Ar$ incremental heating release spectra for 11 individual K-feldspar grains (panels A–K, sample lab ID #27011, aliquots 1 through 11) from core sample 'OGCP-2A-28Y-2 000–010'. Double-barbed arrow indicates the range of heating steps (black boxes) included in the apparent age plateau, with the plateau age given (± 1σ uncertainty). Integrated age (recombined total-gas age) is given at the bottom of each panel.

influence of anomalously old grains on the age population must be mitigated to derive a geologically accurate eruption age. To improve the population sample size in conducting the outlier-elimination procedure described here, all steps belonging to a plateau are used, across all grains of a given sample. Firstly, distinctly older xenocrysts were excluded from the age population based on analysis of the magnitude of age gaps separating older ages from younger (Deino et al., 2018). We employ here an age gap criterion = 7, which efficiently identifies age gaps obvious to a human observer, yet has minimal effect on distributions that lack a visually pronounced modal gap or a prominent shoulder on the older side of the primary distribution. The gap-identification algorithm is followed by outlier deletion based on the normalized median absolute deviation ('nMAD' = 3).

2.3. Tephrocorrelation

Chemical characterization of glass and phenocrysts in core tuff layers has revealed an extensive suite of likely correlations from core to outcrop (McHenry et al., 2020). Correlations are based on EMP analysis of glass shards (where preserved) and phenocryst compositions (feldspar, pyroxene, hornblende, titanomagnetite, ilmenite and aenigmatite, where available). These links are relevant to building an age model of the cores, as eruptive units dated in outcrop can provide additional core chronostratigraphic control elements.

2.4. Paleomagnetic methods

A total of 840 discrete samples were taken from OGCP Cores 2A (500 total) and 3B (340 total) to undertake magnetostratigraphic studies. Approximately 240 of the 2A samples and 295 of the 3B samples were analyzed using a 2-G® Enterprises small-access cryogenic magnetometer with an in-line alternating field (AF) demagnetization coil in the Paleomagnetics Laboratory at the Graduate School of Oceanography at the University of Rhode Island. The initial natural remanent magnetization (NRM) was measured and the samples subjected to 15 AF demagnetization and measurement steps starting at 2.5 mT and ending at 75.0 mT in order to remove any unstable, viscous remanent magnetizations. However, it was observed that the AF demagnetization often produced ambiguous data. For this reason, an additional 260 discrete samples from 2A and 45 discrete samples from 3B were analyzed using thermal demagnetization after measuring the NRM to remove unstable viscous remanent magnetizations. Thermal demagnetization was done with an ASC thermal demagnetizer using 12 steps between 100 and 650 °C. Following measurement, the characteristic remanent magnetization (ChRM) declination and inclination values (Kirschvink, 1980) were calculated using the Demagnetization Analysis in the Excel (DAIE) tool (Sagnotti, 2013). In order to calculate the ChRM, we selected between 4 and 8 demagnetization steps between 5 and 80 mT for AF demagnetization data and between 3 and 8 demagnetization steps between 250 and 600 °C, and a least-squares fit was made to the selected data points. The fit was not anchored to the origin of the Zijderveld plot (Zijderveld, 1967) since the ChRMs generally trended towards the origin without forcing, and we felt the unanchored option gave a better representation of the data quality demonstrated by the maximum angular deviation (MAD) calculated within the DAIE tool. The criteria for a "quality" ChRM value were that it was calculated from at least three consecutive demagnetization steps and that the MAD values were less than 15 (e.g., Tauxe and Badgley, 1988). Data were classified as good, okay, and bad on the basis of the stability of the results on the Zijderveld plot and the MAD values. Good and okay data were used for interpreting the magnetostratigraphy. For Core 2A the results were primarily from samples that were thermally demagnetized, whereas for Core 3B the results were primarily from samples that were AF demagnetized.

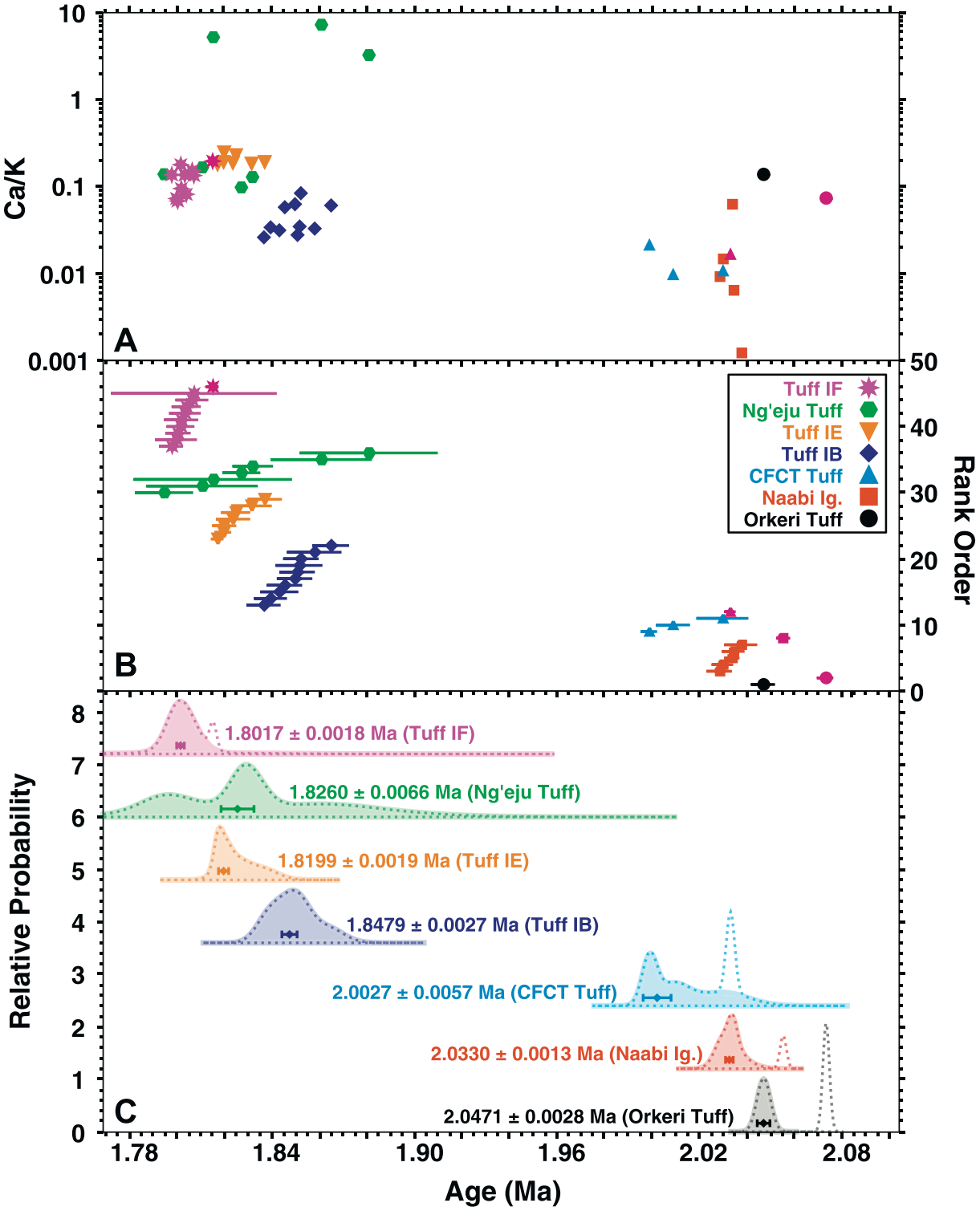

Fig. 3. Aggregated $^{40}Ar/^{39}Ar$ sample ages from core and outcrop for seven volcanic units. A) Ca/K atomic ratio derived as a by-product of the $^{40}Ar/^{39}Ar$ analysis. B) Rank order plot of the individual units. Uncertainties in the age-axis are 1σ standard error. Dark purple markers identify sample ages omitted from the population for the purpose of calculating a best representative age. C) Age-probability density spectra of each unit. Solid line indicates the probability spectrum of the analyses included in the indicated weighted mean age. Dashed curve represents the age-probability spectrum of all ages of a particular unit. (For interpretation of the references to colour in this fig. legend, the reader is referred to the web version of this article.)

Table 1
Mean $^{40}Ar/^{39}Ar$ dating results for volcanic units from combined core and outcrop experiments.

Stratigraphic Unit	Ca/K (median)	Ca/K ± MAD*	*n* included	*n* total	MSWD†	Age (Ma)	± Age 1σ MSE††
HCPT, Bed II¶	0.56	0.75	2	2	0.2	1.879	0.021
Tuff IF, Bed I	0.134	0.050	9	10	0.3	1.8017	0.0018
Ng'eju Tuff, Bed I	0.17	0.17	7	7	3.1	1.8260	0.0066
Tuff IE, Bed I	0.193	0.012	7	7	2.4	1.8199	0.0019
Tuff IB, Bed I	0.034	0.014	10	10	2.2	1.8479	0.0027
Basalt, Bed I	2.6	1.2	5	5	3.1	1.900	0.015
CFCT Tuff	0.0107	0.0017	3	4	4.5	2.0027	0.0057
Naabi Ignimbrite	0.0092	0.0060	5	6	0.9	2.0330	0.0013
Orkeri Tuff	0.138	–	1	2	1.0	2.0471	0.0028
2A-150§	0.19	0.17	2	2	1.8	2.0803	0.0041

* MAD: Median absolute deviation multiplied by 1.4826; an estimator of population standard deviation.
† MSWD: Mean Sqaured Weighted Deviation.
†† MSE: Modified standard error; the standard error expanded by root MSWD if MSWD>1.
¶ "High Calcium Plagioclase Tuff;" age is too old probably due to detrital contamination.
§ Tuff from 147.8–152.7 in Core 2A.

2.5. Bayesian stratigraphic age modeling

Bayesian stratigraphic age analysis is used to construct an age-depth model for OGCP core using *ChronJ* (modification date '2018-04-09'; Keller, 2018; Deino et al., 2019a, 2019b). The prior constraint underlying this analysis is that ages must decrease monotonically stratigraphically upward. The chronostratigraphic data set comprises radiometrically determined tephra-eruption and paleomagnetic-reversal ages, and where appropriate a surface point.

The depositional age of the modern surface is estimated to be 50 ± 50 ka in the models for Cores 2A and 3A. We acknowledge that this number is difficult to quantify and could be in error by some magnitude. At the site of Core 2A the surface is underlain by a meter of so of clayey to sandy soil and regolith, then probable Ndutu Beds, while at 3A the site is immediately underlain by Ndutu sandstone. Thus, apart from a thin veneer of soil at 3A that is negligible in the modeling, the surface strata are in both cases Ndutu Beds. The Ndutu Beds are not well dated, although the situation is improving. In this study, we present a precise $^{40}Ar/^{39}Ar$ age for a tuff sample from 7.01 mbs slightly above the base of the Ndutu in Core 3A of 0.4788 ± 0.0043 Ma (see below). Also, work in progress on outcrop exposures of the Ndutu Beds has resulted in a preliminary $^{40}Ar/^{39}Ar$ age of ~200 ka on a tuff in the Upper Ndutu Beds a few meters beneath the modern surface in the eastern part of the gorge (Deino, pers. comm.). Aspartic acid racemization dating of bone has provided an age of 39 ka on the base of the Naisuisui Beds, which overlie the Ndutu Beds in the gorge, and of 33 and 56 ka for Upper Ndutu Beds (Hay, 1976; Bada, 1985). These ages are consistent with the estimate given above for the uppermost Ndutu surface.

It should be noted that, in contrast to some other Bayesian age-depth models (Blaauw and Christen, 2011; Ramsey, 2008), the approach used here makes no prior assertions regarding the constancy, smoothness, or "memory" of sedimentation rate.

3. Results

3.1. $^{40}Ar/^{39}Ar$ dating

Full $^{40}Ar/^{39}Ar$ analytical data is provided in Table S2 for feldspar from core samples, in Table S3 for feldspar from the First Fault locality at Orkeri, in Table S4 for feldspar from Olduvai Gorge outcrops, and in Table S5 for basalt matrix incremental heating. A total of 4334 SCIH steps on 861 feldspar phenocrysts from 69 samples were analyzed (Table S2); 161 of these grains were rejected as candidates for complete step-heating analysis, after evaluation of one or two low-power steps, due to obviously old xenocrystic ages or high Ca/K content (indicative of plagioclase and an anticipated low-precision result), whereas the remainder were carried to completion (example spectra are provided in Fig. 2).

A dominant proportion of the grains carried to completion in the SCIH experiments yielded apparent-age plateaus (623 out of 700 grains, Table S2). Plateau identification results are provided in Table S6 for feldspar, and Table S7 for basalt matrix. The apparent-age plateaus are plotted as age-probability density functions for each sample in Figs. S1a-c for feldspar from core, in Fig. S2 for the three samples from the Orkeri outcrop locality, and Fig. S4 for the Naabi Ignimbrite from Loc. 67. The age distributions are trimmed to remove xenocrysts and outliers as described in Methods. While most samples exhibit quasi symmetric, unimodal distributions, a significant proportion (about 8–10 of the samples) exhibit marked skewness toward older ages prior to population trimming.

Overall, 68 new $^{40}Ar/^{39}Ar$ Ar ages were obtained from core and outcrop samples: seven from outcrop, 57 from core tuff layers (seven from Core 1A, 32 from Core 2A, and 18 from Core 3A), four from lava (three samples of a single flow in Core 2A, and one from trachyte in Core 3A) (Table S8). Sample weighted-mean ages after application of the outlier-deletion protocol described above are given in Table S9.

3.1.1. Volcanic unit mean ages

Several of the tuffs and the basalts dated directly from core material have also been correlated to outcrop (Table S8) based on tephra geochemistry (McHenry et al., 2020) or unique lithology combined with stratigraphic position (Bed I Basalt). Seven of these units have both new and published $^{40}Ar/^{39}Ar$ ages from outcrop that supplement core dating results (Table S9). Fig. 3 is an age-probability density plot of the available ages aggregated from core and outcrop on a per-unit basis. Applying the same gap-finding routine and outlier deletion methodology described above to these data results in the single oldest age being omitted from Tuff IF, the Coarse Feldspar Crystal Tuff (CFCT), the Naabi Ignimbrite, and the Orkeri Tuff. The resulting distributions are quasi unimodal with reasonable populations (*n* from 5 to 10), with the exception of the CFCT Tuff with just three ages, and the Orkeri Tuff with one (Table 1). The weighted-mean ages of these tuffs provide statistically leveraged values that can be substituted for direct-core dating results in the subsequent age modeling of the cores. The case of the Orkeri Tuff deserves special mention; only two ages are available, one from the core and one from the Orkeri locality (2.073 ± 0.001 and 2.047 ± 0.003 Ma, respectively). Both results are fairly precise, but are statistically distinct at the 95% confidence level. We employ the outcrop age for the Orkeri Tuff in the age modeling (2.047 ± 0.003 Ma) instead of the direct core age, because four of the six samples below the Orkeri Tuff in Core 2A (sample OGDP-2A-44Y-2 015–025, Table S8) yield younger ages (2.068–2.060 Ma) than the core Orkeri Tuff, and we note in section 3.3

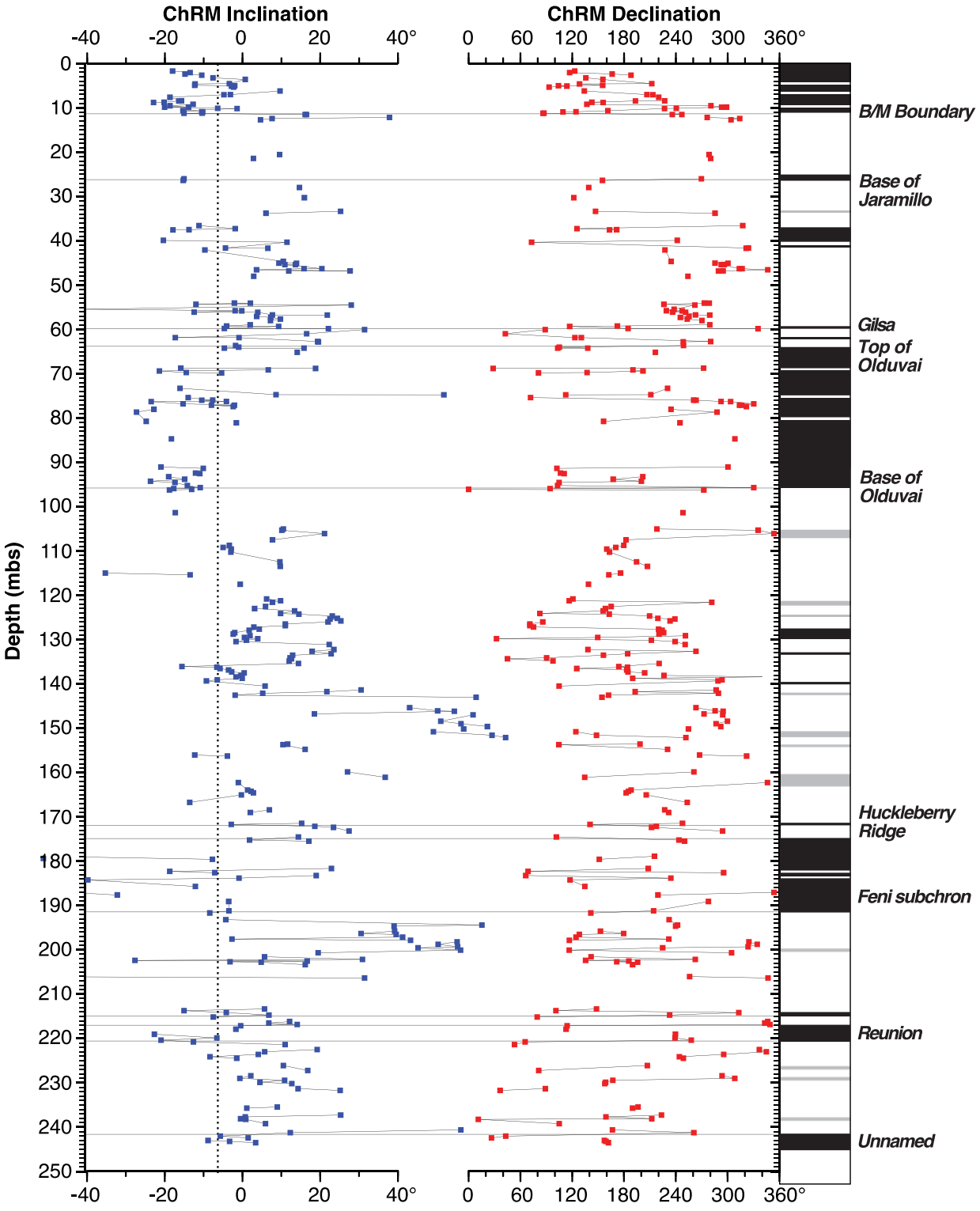

Fig. 4. Characteristic remanent magnetization (ChRM) inclination and declination data for Core 2A. The geocentric axial dipole (GAD) predicted inclination (−6°) for the core site is indicated by the dashed vertical line. The solid horizontal lines represent deviations in declination values in excess of 150° between adjacent samples within a single core. These deviations are interpreted as the normal (black) and reversed (white) boundaries illustrated in the associated polarity fig. and provide the basis for the interpretations presented in this paper. Geomagnetic feature names are from Singer (2014) and references therein.

Table 2
Chronostratigraphic data sets for Cores 1A, 2A, and 3A.

Event Name	Data type*	Age (Ma)	Error in Age ± σ std. er. (Ma)	Core Depth (mbs)	Error in Core Depth (± mbs)†
Core 1A					
HCPT#	Mean ArAr	1.879	0.021	51.55	0.03
1A-19Q-1 082–082	ArAr	1.772	0.028	51.87	0.00
1A-19Q-2 085–092#	ArAr	2.031	0.034	52.98	0.04
1A-21Q-2 081–088	ArAr	1.781	0.012	59.37	0.04
Ng'eju Tuff	Mean ArAr	1.8260	0.0066	61.60	0.03
1A-22Q-2 063–069	ArAr	1.823	0.027	62.10	0.10
Tuff IE	Mean ArAr	1.8199	0.0019	62.40	0.01
Tuff IC	Mean ArAr	1.8481	0.0075	65.05	0.02
Tuff IB	Mean ArAr	1.8479	0.0027	65.65	0.06
1A-25Q-1 100–112	ArAr	1.8344	0.0050	70.11	0.07
Core 2A					
Surface (Top of Ndutu Beds)	Surface	0.05	0.05	1.20	0.01
Brunhes base	Pmag	0.772	0.008	12.00	0.50
Jaramillo base	Pmag	1.071	0.004	26.00	0.50
Gardar	Pmag	1.459	0.009	39.00	2.00
Gilsa	Pmag	1.587	0.008	60.00	0.50
Olduvai top	Pmag	1.770	0.004	64.00	0.50
Tuff IF	Mean ArAr	1.8017	0.0018	66.00	0.30
Ng'eju Tuff	Mean ArAr	1.8260	0.0066	69.88	0.23
Tuff IB#	Mean ArAr	1.8479	0.0027	71.99	0.10
2A-31Y-2 133–135	ArAr	1.8277	0.0083	74.86	0.01
2A-32Y-2 113–116	ArAr	1.8353	0.0081	77.64	0.02
2A-32Y-2 120–121	ArAr	1.841	0.014	77.70	0.01
2A-32Y-2 134–135	ArAr	1.834	0.023	77.84	0.01
2A-33Y-1 079–080	ArAr	1.830	0.032	78.80	0.01
2A-34Y-2 082–084#	ArAr	1.9821	0.0090	83.28	0.01
2A-36Y-2 113–116#	ArAr	2.000	0.011	89.64	0.02
Basalt	Mean ArAr	1.900	0.015	93.20	2.90
Olduvai base unconformity	Pmag	1.9340	0.0080	96.10	0.00
CFCT	Mean ArAr	2.0027	0.0057	97.18	0.98
Naabi Ignimbrite	Mean ArAr	2.0330	0.0013	105.33	1.02
Orkeri Tuff	Mean ArAr	2.0471	0.0028	109.35	1.05
2A-47Y-1 027–037	ArAr	2.0626	0.0032	117.32	0.05
2A-48Y-2 035–044#	ArAr	2.0831	0.0017	121.85	0.12
2A-50Y-2 075–089	ArAr	2.0599	0.0018	128.32	0.07
2A-51Y-2 060–067	ArAr	2.0675	0.0052	131.11	0.12
2A-52Y-2 017–028#	ArAr	2.0953	0.0013	133.70	0.13
2A-53Y-1 134–139	ArAr	2.0675	0.0043	136.37	0.05
2A-54Y-1 096–104	ArAr	2.0799	0.0050	139.00	0.06
2A-55Y-2 113–126#	ArAr	2.0995	0.0036	143.71	0.18
2A-150	Mean ArAr	2.0803	0.0041	150.25	2.45
2A-61Y-1 048–061	ArAr	2.0937	0.0030	156.50	0.05
2A-63Y-2 109–113#	ArAr	2.1371	0.0016	164.61	0.01
2A-64Y-2 027–034	ArAr	2.1227	0.0044	166.73	0.03
Huckleberry Ridge#	Pmag	2.070	0.005	172.00	0.50
Feni top	Pmag	2.115	0.005	175.00	0.50
2A-68Y-1 100–108#	ArAr	2.1632	0.0022	178.08	0.04
2A-72Y-2 028–036	ArAr	2.1480	0.0043	190.78	0.01
Feni base	Pmag	2.155	0.005	192.00	0.50
2A-74Y-2 084–096	ArAr	2.1434	0.0018	196.00	0.08
2A-75Y-2 128–133#	ArAr	2.1754	0.0017	200.76	0.03
2A-76Y-2 016–021	ArAr	2.1671	0.0019	202.72	0.02
Reunion	Pmag	2.200	0.005	218.50	1.50
unnamed/Halawa	Pmag	2.236/2.421	0.005	242.00	1.00
Core 3A					
Surface (Top of Ndutu Beds)	Surface	0.05	0.05	0.00	0.00
3A-04Y-1 088–095	ArAr	0.4788	0.0043	7.02	0.20
Brunhes base/ Jaramillo base	Pmag	0.772/1.071	0.008/0.004	25.5††	0.10
HCPT#	Mean ArAr	1.8790	0.0210	52.40	0.98
Olduvai top	Pmag	1.770	0.004	57.0¶	0.50
Tuff IF	Mean ArAr	1.8017	0.0018	57.63	0.23
Ng'eju Tuff	Mean ArAr	1.8260	0.0066	60.43	0.05
Tuff IE	Mean ArAr	1.8199	0.0019	62.99	2.31
3A-26Y-2 146–149	ArAr	1.8296	0.0062	66.06	0.01
3A-28Y-2 107–111	ArAr	1.8346	0.0062	71.72	0.01
Tuff IC	Mean ArAr	1.8481	0.0075	72.00	0.03
3A-30Y-1 052–054#	ArAr	1.9920	0.1077	75.64	0.01
3A-30Y-1 083–086	ArAr	1.8870	0.0225	75.95	0.02
Basalt scoria (Bed I)	Mean ArAr	1.900	0.015	90.48	1.60
3A-41Y-1 043–044	ArAr	2.0301	0.0030	105.54	0.10
3A-41Y-1 070–080	ArAr	2.0277	0.0030	105.85	0.15
3A-42Y-1 080–089	ArAr	2.0271	0.0031	108.99	0.05
3A-44Y-1 098–108	ArAr	2.0183	0.0030	112.13	0.61
3A-50Y-2 039–047	ArAr	2.0708	0.0040	130.93	0.04
3A-51Y-1 035–042	ArAr	2.1121	0.0035	132.49	0.12

* Data type: 'ArAr'- Table 1; 'Mean ArAr' - Table 2; 'Pmag' - Table _
\# Omitted from preferred Bayesian stratigraphic age model.
† Error in core depth is taken as half the total span of core encompassing the event or possible location of the event.
†† Equivalent to position in Core 3B of 25.82 mbs.
¶ Equivalent to position in Core 3B of 57.56 mbs.

that significant proportion of the core samples are too old relative to stratigraphic age constraints provided by lower core samples.

3.2. Paleomagnetic reversal stratigraphy

The inclination and declination results obtained from the thermally demagnetized samples from Core 2A are shown in Fig. 4. The polarity designation (black/white column) of the samples and the magnetostratigraphic interpretation are also shown. The thermally demagnetized samples were used as the basis of this analysis because they provided more consistent and higher quality results than the AF-demagnetized samples. Unfortunately, the facies associated with deep-water lacustrine intervals did not generally yield good paleomagnetic results irrespective of demagnetization method. Other facies types generally yielded good results. The paleomagnetic polarity transitions are identified in Fig. 4 and are summarized in Table 2.

The paleomagnetic results obtained from Core 3B are shown in Fig. 5. These results were obtained primarily from AF demagnetized samples. We only identified two polarity transitions from this section, the base of the Jaramillo Event and the top of the Olduvai Event as shown in Table 2. More work is needed to further refine the magnetic record of Core 3B. Tephrocorrelation and lithostratigraphic correlation were used to tie the record of Core 3A to Core 3B and integrate the

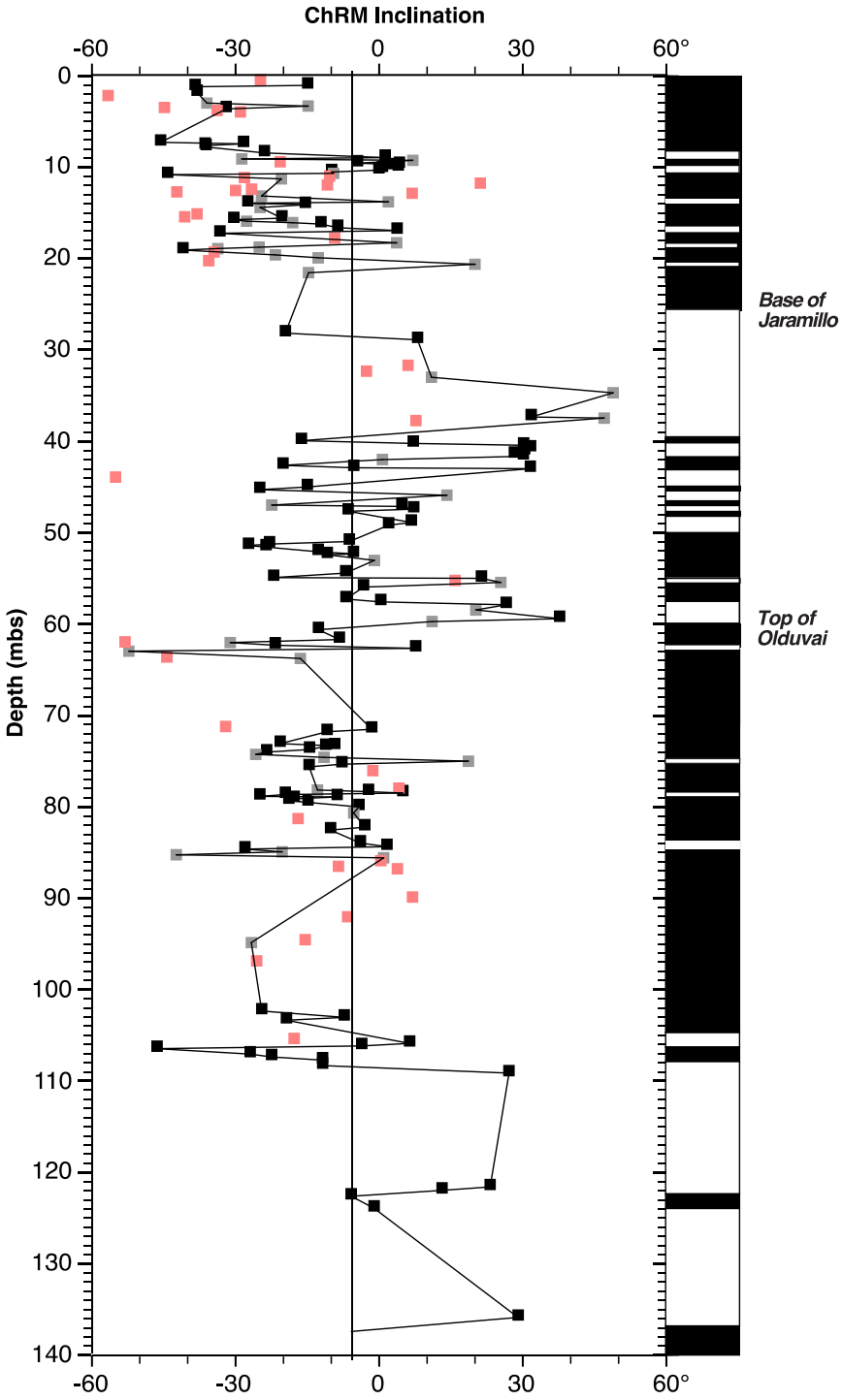

Fig. 5. Characteristic remanent magnetization (ChRM) inclination data for Core 3B. The geocentric axial dipole (GAD) predicted inclination (−6°) for the core site is indicated by the solid vertical line. The black, grey, and red squares indicate "good", "okay", and "bad" data respectively. Although the red squares were classified as "bad", they were included in the fig. to provide limited constraints in intervals of low data density. (For interpretation of the references to colour in this fig. legend, the reader is referred to the web version of this article.)

magnetic results from Core 3B with the dating studies done on Core 3A (Table 2).

3.3. Bayesian stratigraphic age modeling

Table 2 shows the final set of chronostratigraphic data supporting Bayesian age models for the OGCP cores, consisting of four data types: (1) $^{40}Ar/^{39}Ar$ ages obtained directly from individual core samples; (2) $^{40}Ar/^{39}Ar$ overall mean ages of correlated outcrop and core volcanic units; (3) paleomagnetic reversal boundaries; and (4) modern surface points. Sufficient data are available for 1A, 2A, and 3A to construct age models. The model for 1A extends from ~70–52 mbs, and for 3A from ~134–0 mbs. 2A is divided into two separate models due to the presence of a major unconformity at the Bed I Basalt/CFCT contact (Stanistreet et al., 2020a, 2020b, 2020c): one for the bottom two-thirds from ~242–96 mbs, and another for the upper strata from 96 to 0 mbs. We discuss model development for Core 2A first because it offers the most complete section, followed by discussion of Cores 1A and 3A.

The development of an age model for the strata below the sub-basalt unconformity in Core 2A is illustrated in Fig. 6. Panel 'A' shows the

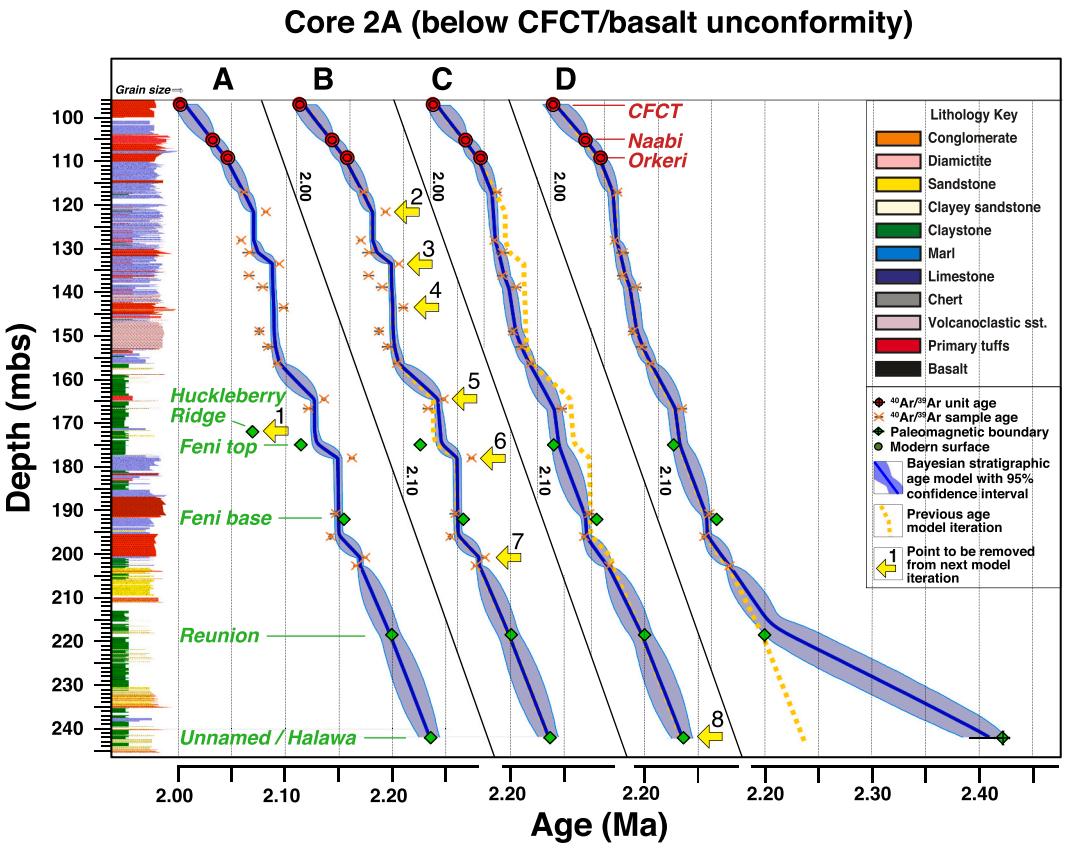

Fig. 6. Development of a Bayesian stratigraphic age model for Core 2A below the unconformity at the base of the basalt at 96 mbs. Model A incorporates all available chronostratigraphic control points. Model B is generated from the data set after removal of the anomalous 'Huckleberry Ridge' paleomagnetic normal event (yellow arrow #1). Model C, the preferred model for this lower part of Core 2A, results from removal of six $^{40}Ar/^{39}Ar$ sample ages that are anomalously old (yellow arrows #2–7) (Table S10). Model D is a speculative model resulting from re-interpretation of the lowermost paleomagnetic event as an older excursion (yellow arrow #8). (For interpretation of the references to colour in this fig. legend, the reader is referred to the web version of this article.)

result obtained using all the data available for this interval (Table S10A). While most of the data support the overall model result, it is clear that several chronostratigraphic control points are incongruous. For example, the datum based on the Huckleberry Ridge paleomagnetic excursion at 2.070 Ma (identified by arrow #1 in Fig. 6) is too young by ~60 kyr when considered in the context of the new core radiometric ages, and the identification of the Feni top paleomagnetic excursion just three meters below. There are several possible explanations for the anomalous 'Huckleberry Ridge' normal: 1) the published age (Singer, 2014) is too young, 2) it is a modern overprint, or 3) it belongs to an unrecognized excursion.

We omit this point in the next iteration of the age model (Fig. 6b; Table S10B). This, and the previous model, reveals a series of potential age anomalies, manifested by sharp bends induced by relatively old, precise ages, flanked by younger ages. We believe these older ages are influenced by the presence of excess ^{40}Ar, with perhaps a reworking component. Excess ^{40}Ar has been noted previously in Ngorongoro eruptive units (i.e., the CFCT; Deino, 2012), and may be an episodic manifestation in this volcanic system, in contrast to the Olmoti-derived products of mid to upper Bed I. We identify anomalously old sample results as those $^{40}Ar/^{39}Ar$ ages whose 95% confidence intervals are older and do not overlap with the 95% confidence interval of the age model at the stratigraphic height of the sample (Table S8, Table S10B). This identifies six suspect results (arrows 2–7 of Fig. 6b).

Fig. 6c shows a model with these points removed; as anticipated, the major kinks in accumulation rate are smoothed. Model C is essentially the same as B in the initial ~30 m and final 40 m, but is younger than B through the middle portion of the model, with a maximum difference of 25 kyr at 178 mbs (median overall difference is 6 kyr). This model (C) is taken as the preferred result for Core 2A below the CFCT/basalt unconformity (Table S10C).

The oldest chronostratigraphic datum in 2A (the paleomagnetic excursion at 242 mbs) is just 3.2 m above the bottom of the core. Extrapolating age model C to this end point using the last two paleomagnetic excursions yields an age of 2.24 Ma for the base of the lacustrine beds at the bottom of the core. These are the oldest deposits so far recognized in the Olduvai Beds, about 210 kyr older than the 2.033 Ma Naabi Ignimbrite exposed in outcrop at Olduvai Gorge, and about 190 kyr older than the 2.0471 Ma Orkeri Tuff exposed along the First Fault.

Finally, we note an alternative model based on re-assignment of the normal paleomagnetic event identified at the bottom of Core 2A, attributed in model C to an unnamed excursion at 2.236 Ma, to the older Halawa excursion at 2.421 Ma (both being astrochronological ages from Laj and Channell, 2007) (arrow #8). A model based on this interpretation is shown in Fig. 6d. While possible, this model exhibits an abrupt shallowing of accumulation rates (~13 cm/kyr) from ~215 mbs to the bottom of the core, whereas model C shows an accumulation rate consistent with the overall core rate (63 cm/kyr). This change in sedimentation rate is not supported on lithologic grounds; the primarily fine-grained lacustrine interval from 153 to 173 mbs (the upper Naibor Soit Formation), similar lithologically to the lower interval from 213 to 244 mbs (lower Naibor Soit Formation), exhibits the typically high sedimentation rate (~61 cm/kyr) characteristic of Core 2A below the unconformity. We favor the simpler model and accept C as the best approximation of the sediment accumulation curve for the lower part of Core 2A.

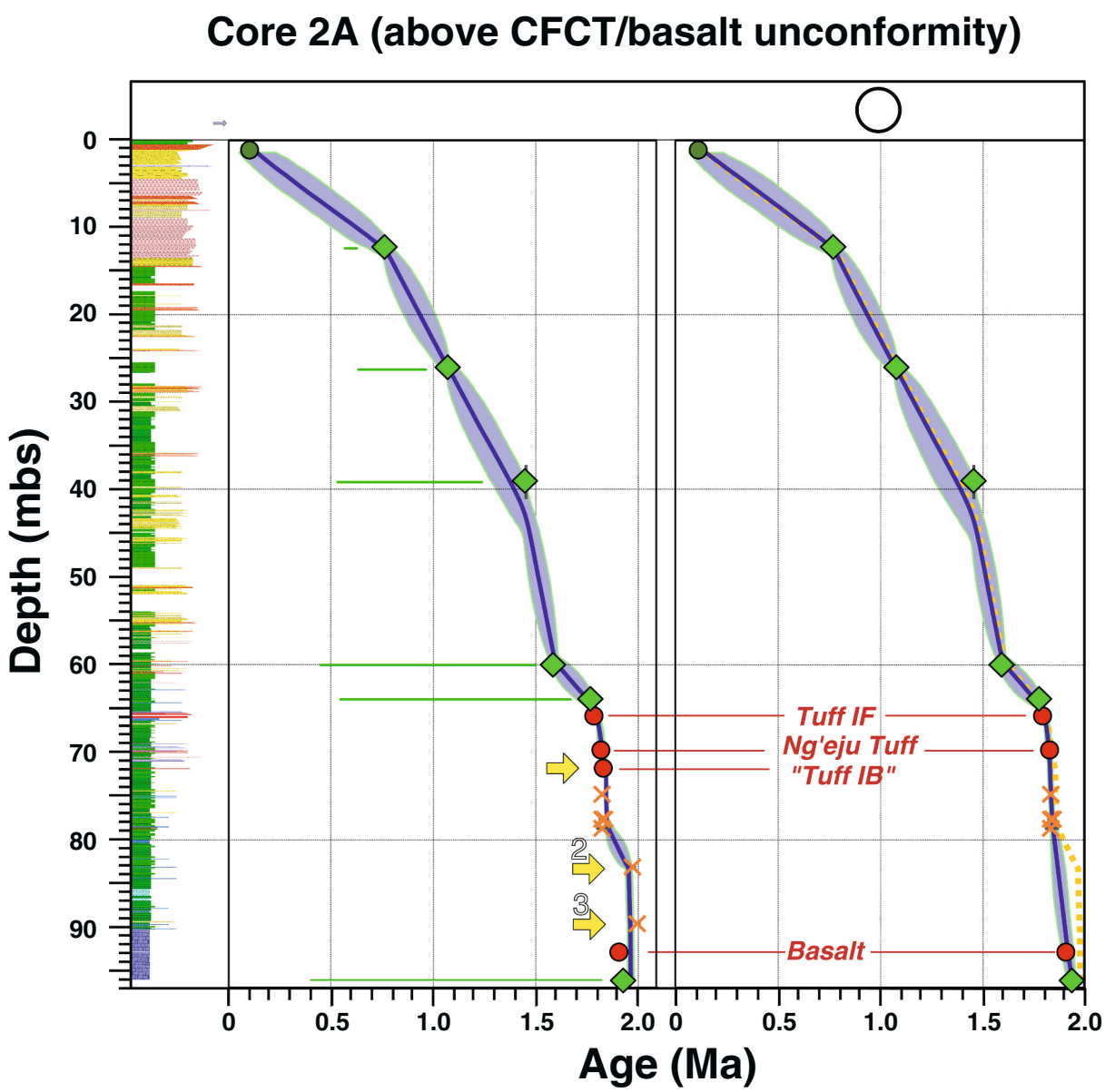

Fig. 7. Development of a Bayesian stratigraphic age model for Core 2A above the CFCT/basalt unconformity at 96 mbs. Model A incorporates all available chronostratigraphic control points. Model B is generated from the data set after removal of a postulated Tuff IB correlation that is at odds with direct core dating results (yellow arrow #1), and two core ages that are anomalously old likely due to detrital contamination (yellow arrows #2 and 3). Model B is then the preferred result for the upper part of Core 2A. (For interpretation of the references to colour in this fig. legend, the reader is referred to the web version of this article.)

Fig. 7 shows the development of a Bayesian stratigraphic age model for Core 2A above the CFCT/basalt unconformity. The initial model (A in Fig. 7; Table S11A) is based on four mean unit $^{40}Ar/^{39}Ar$ ages (the basalt flow at 90–96 mbs, Tuff IB, Ng'eju Tuff, and Tuff IF; Table 1), seven individual core sample $^{40}Ar/^{39}Ar$ ages, six paleomagnetic boundaries or excursions (Olduvai base, Olduvai top, Gilsa, Gardar, Jaramillo base, and the Brunhes base), and a surface point. There are, however, three components of the chronostratigraphic data set that are anomalous when taken in the context of the overall section. Firstly, the two individual core sample ages of 1.982 ± 0.009 and 2.000 ± 0.011 Ma at 83.28 and 89.64 mbs, respectively, are older than the underlying basalt (1.956 ± 0.031 Ma) and the base of the Olduvai event (1.934 ± 0.008 Ma; Simon et al., 2018), which coincides with the sub-Bed I basalt unconformity at 96 mbs. These older feldspars are likely attributable to reworking of older Ngorongoro Volcano ejecta, as is commonly encountered when attempting to date lower Bed I volcaniclastic deposits (Deino, 2012). These two samples (2A-34Y-2 082–084 and 2A-36Y-2 113–116) are omitted from the next iteration of the age model. Also, a 6 cm thick layer in Core 2A at 71.99 mbs has tephra geochemistry similar to Tuff IB (McHenry et al., 2020) and is included in this initial model, but the mean age of confirmed outcrop samples of Tuff IB (1.8479 ± 0.0027; Table 1) is older than five underlying, directly dated core samples from 78.80–74.68 mbs (age range 1.8297 to 1.8414 Ma). It should be noted these samples are as much as seven meters below the proposed Tuff IB tuff, adding a maximum of 18 kyr to the discordancy based on this iteration of the model. As the age of Tuff IB is well-constrained by multiple consistent outcrop ages (Table 1), we suspect the proposed correlation is incorrect. A final model, B, is calculated omitting the Tuff IB correlation, and the two detritally contaminated samples (Fig. 7b; Table S11B). This is the preferred Bayesian age model for Core 2A above the CFCT/Basalt unconformity.

The development of an age model for Core 1A is fairly simple, as we

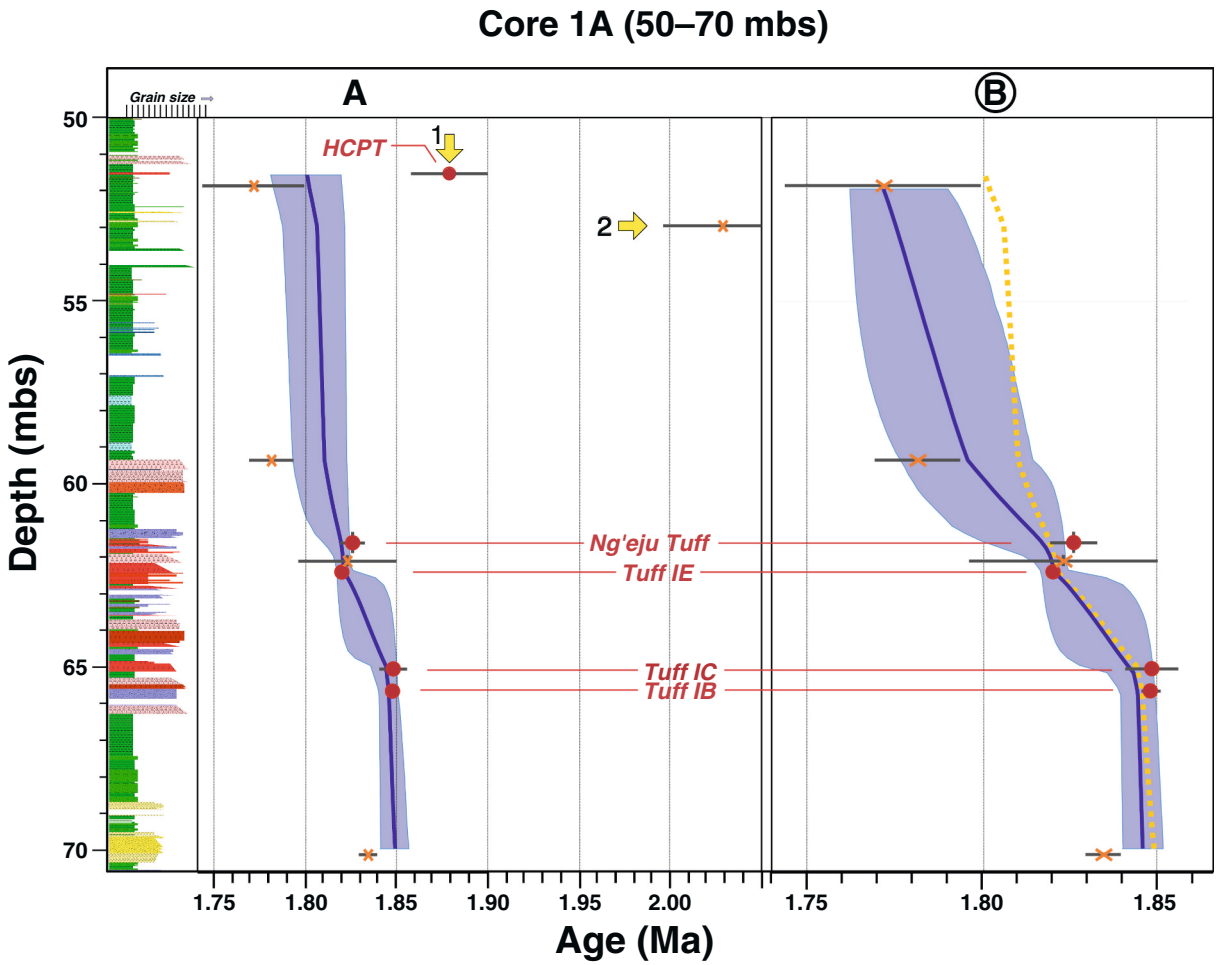

Fig. 8. Development of a Bayesian stratigraphic age model for Core 1A from 50 to 70 mbs. Model A incorporates all available chronostratigraphic control points. The preferred result, Model B, results from removal of two $^{40}Ar/^{39}Ar$ data points interpreted as anomalously old due to detrital contamination (yellow arrows #1 and #2). (For interpretation of the references to colour in this fig. legend, the reader is referred to the web version of this article.)

consider here a relatively short portion of the core (50–70 mbs) for which we have chronostratigraphic control (10 points comprised of individual $^{40}Ar/^{39}Ar$ core ages, and mean unit $^{40}Ar/^{39}Ar$ ages). A model incorporating all data is shown in Fig. 8a (Table S12A). Two control points are anomalously old; the mean age for the High Calcium Plagioclase Tuff (HCPT; McHenry et al., 2020) at 51.55 mbs is ~100 kyr too old, reflecting dominance of the K-feldspar population by old detrital grains; likewise the $^{40}Ar/^{39}Ar$ age from a core sample from 51.87 mbs also reflects detrital contamination. Removal of these points from the set yields the preferred age model shown in Fig. 8b (Table S12C).

Model development for Core 3A is shown in Fig. 9. This core extends from 134 mbs at ~2.1 Ma, to the modern surface, and is calibrated with a total of 20 chronostratigraphic control points from all four categories. Note that this includes a datum for the lower Bed I basalt flow sequence dated in Core 2A and in outcrop, based on identification of three closely spaced scoria-bearing horizons in Core 3A at ~90 mbs (Stanistreet et al., 2020a, 2020b). A stratigraphic model with all control points is shown in Fig. 9a (Table S13A). As was the case with Core 2A, the age for the HCPT is anomalously old due to detrital contamination (yellow arrow #1). Another tuff at level 75.64 mbs (3A-30Y-1 052–054; yellow arrow #2), is also too old, as its 95% confidence level does not overlap with the 95% confidence level of the Bayesian model at this stratigraphic level (Table S8, Table S13A). Removal of these two points yields model B (Table S13B). This includes a control point based on identification of the base of the Brunhes paleomagnetic boundary at 25.82 mbs (yellow arrow #3). While this is a valid model that fits the available chronostratigraphic data, we feel re-interpretation of this transition as the base of the Jaramillo (model C) provides a better fit to the overall geological data for three reasons: 1) this change removes an inflection to the accumulation curve forced by the relatively young age of the Brunhes at point #3, making the curve a better match for the stratigraphic age model for Core 2A which records both the Brunhes and Jaramillo lower bounds (upper, Fig. 7); 2) the depth of the Jaramillo base in Core 2A is 26.0 mbs, and in Core 3A we are proposing a nearly identical 25.8 mbs; 3) the lithostratigraphic sequences of cores 2A and 3A are very similar in the upper parts; the sharp junction between Bed IV claystones and coarse detrital facies ('Masek Beds') occurs at ~14.5 mbs in 2A and 12.2 mbs in 3A, and we infer that this is roughly isochronous between the two cores. We take model C as the preferred Bayesian stratigraphic age model for Core 3A (Table S13C).

4. Discussion

4.1. Comparative chronologies of Cores 2A and 3A

A comparison of the age models between Cores 2A and 3A reveal details of the northeast-southwest stratigraphic relationships throughout the Olduvai Basin-fill (Fig. 10). Structurally, both coring sites lie in the same fault block (between the Fifth and FLK faults), and lie along the same general southwest-northeast trend of the East African

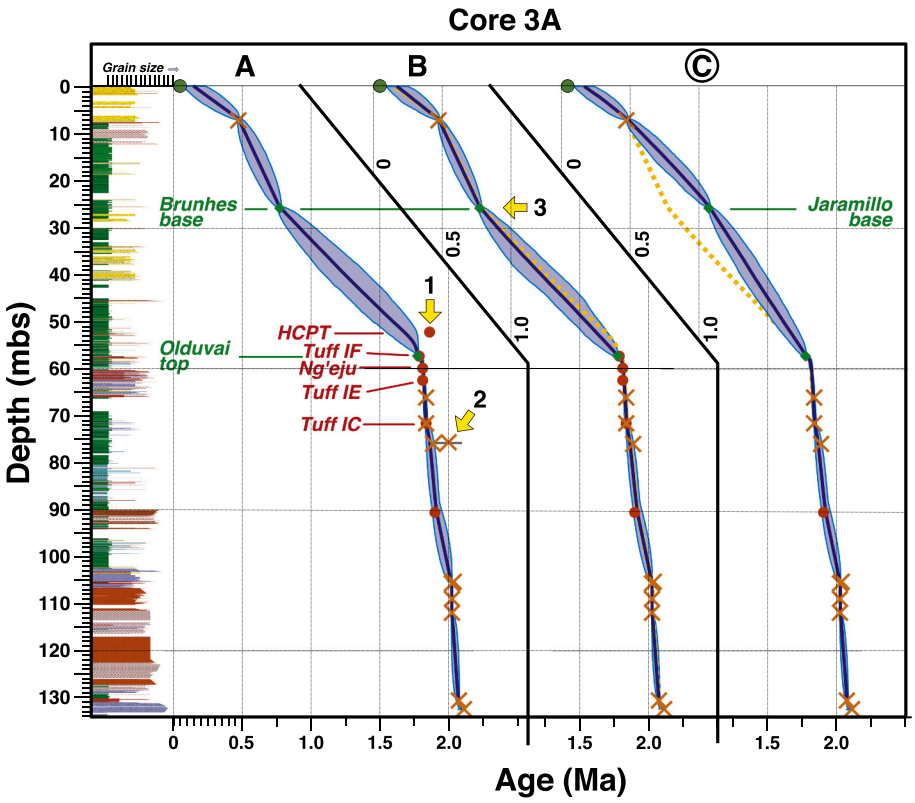

Fig. 9. Development of a Bayesian stratigraphic age model for Core 3A. Model A incorporates all available chronostratigraphic control points with the exception of a tentative Tuff IID correlation. Model B is generated from this data set after removal of two $^{40}Ar/^{39}Ar$ data points interpreted as anomalously old due to detrital contamination (yellow arrows #1 and 2). Model C is based on re-interpretation of a reverse-to-normal upward paleomagnetic transition at 25.82 mbs as the base of the Jaramillo (yellow arrow #3), rather than the base of the Brunhes. This result (C) is the preferred Bayesian stratigraphic age model for Core 3A. (For interpretation of the references to colour in this fig. legend, the reader is referred to the web version of this article.)

rift system in this region, and the adjacent NVH to the southeast (Fig. 1). 3A lies 7.3 km northeast of 2A, and is ~5 km closer to the Olmoti volcanic source, whereas 2A and 3A are both directly downslope and virtually equidistant from Ngorongoro Caldera (Fig. 1).

The early part of Core 2A has no temporal equivalent in Core 3A. This unique opportunity to examine the early basin history reveals the predominance of mainly lacustrine strata, with fluvio-deltaic deposition of the Naibor Soit Formation (Stanistreet et al., 2020a) between 156 and 245 mbs, interrupted by several thick sequences of Ngorongoro-derived pyroclastic deposits from 177 to 201 mbs (the 'lower pulse' of the Ngorongoro Formation from 2.16–2.12 Ma).

Despite their similar physiographic relationship to the Ngorongoro Caldera in the NVH highlands, cores 2A and 3A show significant differences in the accumulation of lacustrine versus pyroclastic fan deposition in early core histories. These relationships are discussed in detail in Stanistreet et al. (2020a), who identify site 2A as situated higher on a Ngorongoro fan-delta extending northwestward from the Ngorongoro volcanic edifice, whereas site 3A is situated in a more distal, lake-dominated environment. Above the level of the lower pulse of the Ngorongoro Formation, cores 2A and 3A contain equivalent aged strata, in both cores almost exclusively consisting of volcanic materials of the Ngorongoro Formation ('upper pulse,' from ~2.11–2.00 Ma, between the black dotted lines of Fig. 10). While the base of the upper pulse was not reached in core 3A (i.e., the anticipated Naibor Soit Formation was not reached beneath the trachyte flow at the base of 3A), an isochronous line linking 3A and 2A at 2.11 Ma (black dotted line in Fig. 10) shows that the contemporaneous Ngorongoro Formation sequence in 2A is much thicker (62 m) than in 3A (22 m), supporting the notion that the axis of the Ngorongoro pyroclastic fan was deflected northeastward within the deepest depository.

The age models for 2A and 3A are well constrained by $^{40}Ar/^{39}Ar$ control points near the upper boundary of the Ngorongoro Formation, and give nearly the same age for the boundary, 2.01 and 2.00 Ma, respectively. Despite their virtual age equivalence at this contact, the subsequent histories of these cores are markedly different. An unconformity of ~11 kyr exists between the CFCT tuff at the top of the Ngorongoro Formation in Core 2A and emplacement of the basaltic lava flows of Bed I. Core 3A reveals mainly lacustrine strata of Lower Bed I in the interval below the position of the basalt, again indicating that the sediment surface recorded in core 3A was topographically low at 2.01–2.00 Ma, relative to the higher fan surface topography recorded in Core 2A.

The core positions of the top of the interval of Bed I Basalt flows and ash falls are nearly identical in 2A and 3A, at 90 and 91 mbs, respectively. By this time, eruptive activity at Ngorongoro had terminated, while the locus of activity in the NVH was due to the shift to Olmoti Volcano during Upper Bed I. The progradation of the Olmoti fan-delta into the Olduvai Basin is documented in detail elsewhere (Hay, 1976; McHenry, 2005; Stollhofen et al., 2008; Stollhofen and Stanistreet, 2012). Cores 1A, 3A and 3B are situated in the more proximal Olmoti fan-delta position, while 2A is situated at the distal toe of the delta-fan as it enters Paleolake Olduvai (Stanistreet et al., 2020a), and deposits from this center contributed to unequal rates of accumulation between the sites. The top of Bed I (Tuff IF at 1.8017 Ma) is 66 mbs in 2A and 57 mbs in 3A, the difference of 9 m being largely attributable to a thick wedge of Olmoti fan-delta deposits between 60 and 66 mbs in 3A.

By the end of Bed II, core depths are again nearly equal at 28–29 mbs due to greater net accretion in Core 2A than 3A. All final age-stratigraphic models for Bed II (Cores 1A, 2A, and 3A; Figs. 6-9) indicate an early period of relatively slow accumulation, followed by higher rates more typical of the core as a whole. Unfortunately, few chronostratigraphic data points are available in Bed II to provide finer resolution.

The Bayesian stratigraphic models for Cores 2A and 3A provide age estimates for the basal contacts of the succeeding Olduvai Gorge stratigraphic units (Bed III, Bed IV, Masek, and Ndutu; lithologic boundaries provided in Stanistreet et al., 2020a) (Table 3). The base of Bed III is nearly level between Cores 2A and 3A, and is found in both cores a few

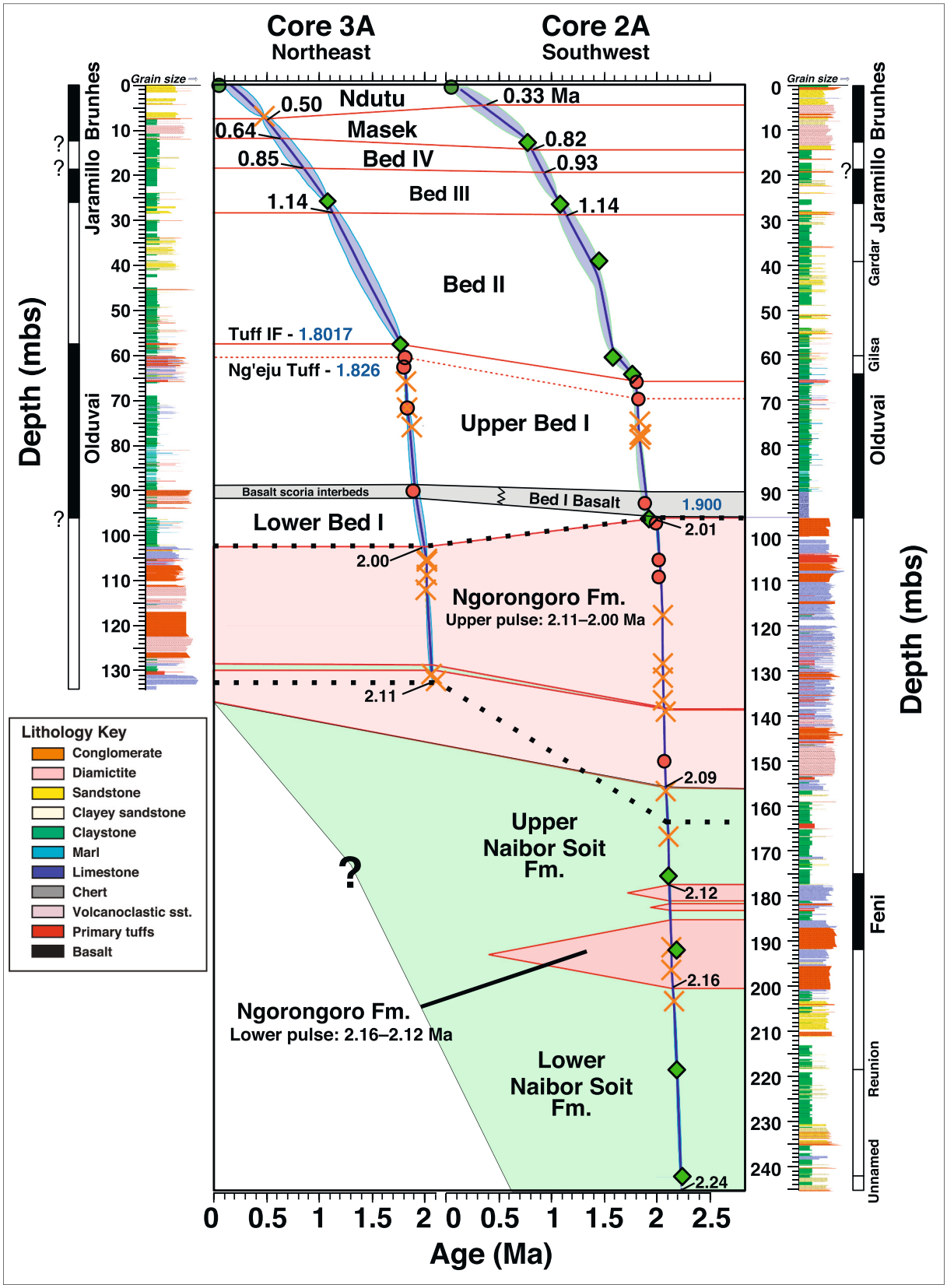

Fig. 10. Comparison of the stratigraphy and age models for Cores 2A and 3A, in the context of the lithostratigraphic framework defined by Stanistreet et al. (2020a). Magnetostratigraphy, depth scale, and lithostratigraphy are shown on the left for 3A, and on the right for 2A (depth scaling is the same for both cores). Age models and chronostratigraphic data sets are the preferred results, as indicated in Figs. 6 and 7 for 2A, and in Fig. 9 for 3A. All numbers within the main body of the fig. are ages in Ma; those in black are derived from the age models, while those in blue are $^{40}Ar/^{39}Ar$ unit ages (Table 1). (For interpretation of the references to colour in this fig. legend, the reader is referred to the web version of this article.)

Table 3
Stratigraphic boundary ages.

Stratigraphic Unit (base unless noted)	Basal Contact (mbs)	Model Age (Ma)	Model Age Error (± 95% CI)	Accumulation Rate (cm/ka)*
Core 2A				
Ndutu (Top)	1.2	0.14	0.08	–
Ndutu (Base)	4.7	0.33	0.13	1.93
Masek	14.7	0.82	0.06	2.21
Bed IV	19.6	0.93	0.08	4.34
Bed III	29.0	1.14	0.07	4.50
Bed II	66.0	1.800	0.016	5.59*
Upper Bed I	90.2	1.90	0.033	23.85
Lower Bed I	96.0	1.937	0.018	14.64
Ngorongoro Fm (upper pulse)	156.4	2.093	0.006	39.57
Naibor Soit Fm (upper)	177.2	2.124	0.010	68.84
Ngorongoro Fm (lower pulse)	201.0	2.162	0.009	61.70
Naibor Soit Fm (lower)	245.2	2.24†	–	56.84
Core 3A				
Surface (Ndutu)	0.0	0.16	0.07	–
Ndutu	7.8	0.50	0.04	2.27
Masek	12.0	0.64	0.09	2.90
Bed IV	18.6	0.85	0.09	3.18
Bed III	28.6	1.14	0.06	3.76
Bed II	57.6	1.801	0.014	4.32
Upper Bed I	88.9	1.91	0.03	25.70
Lower Bed I	102.4	2.00	0.03	14.57
Ngorongoro Fm (upper pulse)	132.49	2.109	0.015	28.35

* Calculated between the midpoints of stratigraphic units.
† Extrapolation of model to the bottom of 2A.

meters below the lower Jaramillo paleomagnetic transition. This provides convenient chronostratigraphic control, leading to identical model ages in both cores for the base of Bed III of 1.14 Ma (Table 3). The base of Bed IV is not as tightly controlled chronostratigraphically, and the ages for 2A and 3A differ by 70 kyr at 0.93 and 0.86 Ma; however, the 2A result is better constrained between the base of the Jaramillo and Brunhes paleomagnetic chrons (95% confidence intervals are ±0.08 and ± 0.09 Ma for 2A and 3A, respectively). The base of the Masek beds is well constrained temporally at 0.82 Ma by the base of the Brunhes paleomagnetic transition just one meter above in Core 2A; however, the base of the Brunhes was not identified in 3A, and the resulting model age for the base of the Masek is ~120 kyr younger at 0.64 Ma. The age of the base of the Ndutu in Core 3A is tightly controlled by direct $^{40}Ar/^{39}Ar$ dating of a tuff just above the contact, yielding a model age of 0.50 Ma, while in Core 2A this contact is relatively poorly constrained and yields a model age of 0.35 Ma. We also acknowledge the possibility that the cores exhibit different stratigraphies involving upper and lower Ndutu beds, and that this younger age in 2A is potentially real. Time-transgressive contacts are certainly a likelihood for all of the basal contacts of stratigraphic units above Bed II. Nevertheless, we list here preferred ages based on the best constraints: the base of Bed III is 1.14 ± 0.05 (95% confidence interval; the mean of 2A and 3A), Bed IV is 0.93 ± 0.08 (2A), Masek is 0.82 ± 0.06 (2A), and Ndutu is 0.50 ± 0.04 Ma (3A).

Net accretion rates for 2A and 3A are plotted against core depth and age in Fig. 11. These plots reveal relatively high accumulation rates in the deepest core depths of ~57–69 cm/kyr encompassing the lower Naibor Soit, lower Ngorongoro, and upper Naibor Soit Formations. However, by upper Ngorongoro Fm. time, rates begin a steep decline ultimately reaching order-of-magnitude slower accumulation following Upper Bed I. This decline was initiated over a short interval of only ~100 kyr between the midpoint of the upper Naibor Soit and upper Ngorongoro Formations. By the time of Lower Bed I deposition, rates had fallen to approximately one fourth of their highest value, in only ~250 kyr. Upper Bed I saw an uptick in accumulation rates in both cores, before falling sharply again for the remainder of the stratigraphic sequence. It should be noted that the sharp rate transitions in Core 2A occur during the time of greatest activity of Ngorongoro Volcano, a large edifice with a present caldera diameter of 22 × 18 km. Volcano-tectonic deformation associated with the build-up in activity of Ngorongoro may feature in rapid changes in Olduvai Basin architecture at this time. Actual sedimentation rates might be considerably higher if decompaction of strata and unconformity surfaces with variable degrees of downcutting and sequence removal are considered.

Overall, the net strata accumulation rates for Cores 2A and 3A are 11 and 6 cm/kyr, the difference being attributable to the greater maximum depth of 2A incorporating high accumulation rate sequences. By comparison, the 1 Ma Magadi and Koora basins 159 and 176 km to the northeast within the rift valley have overall rates of 19 and 15 cm/kyr, respectively (Owen et al., 2019; Deino et al., 2019a). Therefore, while the long history of the Olduvai Basin includes an early phase of high accumulation that greatly exceeds the average rates of nearby rift basins, overall the Olduvai Basin has experienced generally waning sedimentation over the past two million years, resulting in comparatively low mean accumulation rates.

Results from the OGCP demonstrate that the Olduvai Basin sedimentary and volcanic stratigraphy continues well below the present limits of the gorge. Core 2A recovered an additional 140 m of strata beneath the oldest exposures, reaching a model age of 2.24 Ma at 245 mbs. Seismic surveys of the basin suggest there may be another 135 m of strata at 2A beneath deepest level drilled (Lu et al., 2019); extrapolating Core 2A accumulation rates for the Naibor Soit and Ngorongoro Formations suggests that the oldest sedimentary strata in the Olduvai Beds beneath this site may be ~2.5 Ma.

4.2. Magmatic and erosional history

The SCIH $^{40}Ar/^{39}Ar$ analyses reported here, performed with the primary goal of quantifying the eruptive age of tuffs and flows in the OGCP cores, can also be applied to the broader purpose of examining the regional volcanic and erosional history of the Olduvai Basin. As described, many of the tuffs from the core bear xenocrystic feldspar, older than the true eruption age, either derived from the magma itself, or entrained during pyroclastic or fluvial transport to the site of deposition in the OGCP cores. Excess ^{40}Ar in primary feldspars is also prominent in some of these tuffs. While this later anomalous-age component is not particularly helpful in defining the prior volcanic history, the departure from a primary age due to this source is usually small relative to the broad age scope considered here.

Fig. 12 is an age-probability density plot of integrated ages derived from the feldspar SCIH experiments from the cores. Integrated ages are calculated by recombination of the isotope measurements for all steps from a single grain, thus are similar to a total-fusion measurement. The data have been filtered to exclude results with large age uncertainties (> ± 0.1 Ma, e.g., from high-Ca plagioclase), to highlight details provided by the more precise, lower Ca ages. The probability distribution is dominated by two peaks: 'C' from ~2.2–1.9 Ma representing eruptive activity from Ngorongoro Volcano, starting with the lowest tuff layers in Core 2A (~201 mbs) up through the top of the CFCT (96 mbs); and 'B' from 1.9–1.7 Ma derived from the eruptive activity of Olmoti Volcano, from sample 2A-33Y-1 079–080 up through Tuff IF (~79 to 66 mbs in Core 2A). A much smaller peak ('A' at 0.49 Ma) is from a single tuff encountered in Core 3A (sample 3A-04Y-1 088–095, 7.02 mbs) with an age of 0.4788 ± 0.0043 Ma, likely also sourced from the NVH. Small peaks in the distribution on the old-age shoulder of the Ngorongoro distribution (D at ~2.3–2.2 Ma) may represent pyroclastic activity from Lemagrut (Fig. 1), as recorded at this approximate time at nearby Laetoli as the Olgol Lava and at Naisuri Gorge as a thick tuff (Deino, 2011; McHenry and Deino, 2020). A small peak at ~2.63 Ma ('E') could be representative of the Upper Ndolanya Beds at Laetoli (Deino and

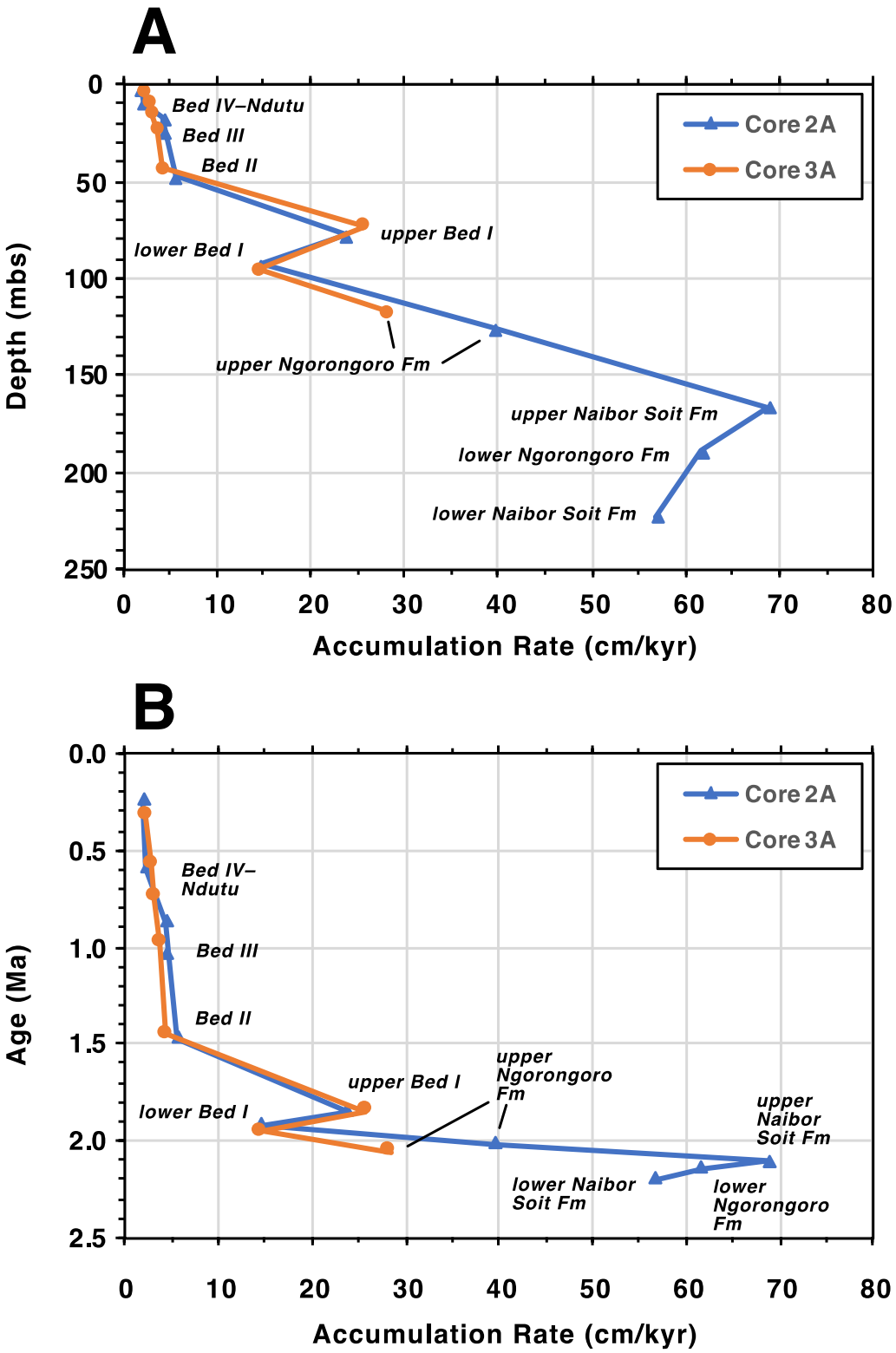

Fig. 11. Net accretion rates for Cores 2A and 3A plotted against depth (A) and age (B). The depth plotted is the midpoints of the stratigraphic units as encountered in the core, and the ages are the average of the top and bottom contacts of each unit.

Harrison, 2011); and at ~3.8–3.7 Ma ('F') may be tied to activity of Sadiman which gave rise to the Upper Laetolil Beds (3.85–3.63 Ma; Deino, 2011). It is perhaps surprising that older feldspars predating Ngorongoro activity are not more common in the observed probability distribution; this may reflect an absence of deep erosion of earlier strata within the Olduvai Basin drainage.

Another interesting aspect of this overall view of the feldspar phenocryst composition of the dated samples is that it may provide insights into the magmatic evolution of Ngorongoro Volcano. Distribution C mainly comprises grains with Ca/K ratios from 0.01–0.1, which are low K sanidine to anorthoclase. High-K sanidine, with Ca/K ratios less than 0.01 are not erupted until the final phases of Ngorongoro activity

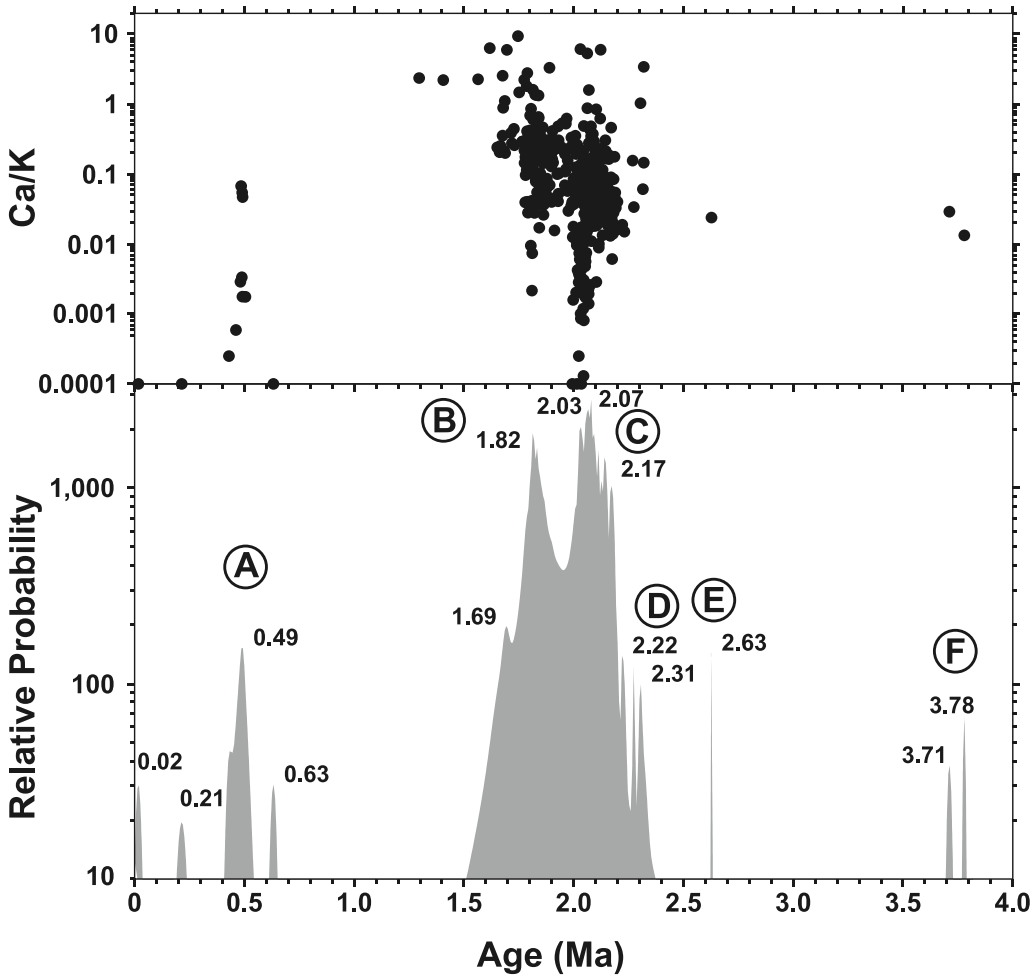

Fig. 12. Age-probability density function of integrated ages from SCIH core feldspar experiments. The relative probability at a given age roughly approximates the frequency of the age of feldspar phenocrysts in core tuffs, although distortions occur due to varying numbers of grains analyzed per sample and incomplete sampling of tuff units. 607 grains are represented, derived from the integrated ages of incremental heating experiments, or from two-step analyses at low temperature where grains were considered too old to necessitate completion of the incremental heating sequence. The circled letter annotations (A–F) identify various components of the distribution as discussed in the text. The atomic Ca/K ratio plotted in the upper panel is derived from the $^{37}Ar/^{39}Ar$ total-gas composition.

(e.g., the Naabi Ignimbrite). This may reflect magma evolution processes leading to the generation and eruption of more highly differentiated magmas only toward the terminus of activity of this center.

5. Conclusions

We have employed $^{40}Ar/^{39}Ar$ dating of tuffs and lavas, magnetostratigraphy, and tephrostratigraphy to obtain a suite of age-calibration points from three of the OGCP cores collected from the Olduvai Basin in 2014 (1A, 2A, and 3A). In addition, we applied $^{40}Ar/^{39}Ar$ dating to select relevant outcrops in the Olduvai Basin to supplement core data. We then used the resulting chronostratigraphic data set to constrain a series of Bayesian stratigraphic age models for the cores.

These models yield age estimates for the upper Olduvai Gorge stratigraphic units (Bed III, Bed IV, Masek, and Ndutu) that have been difficult to date in the past due to the paucity of suitable material for radiometric dating and the absence of detailed magnetostratigraphic investigations. The preferred ages for the basal contact of these units based on the best model constraints are: Bed III at 1.14 ± 0.05 (95% confidence interval), Bed IV at 0.93 ± 0.08, Masek at 0.82 ± 0.06, and Ndutu at 0.50 ± 0.04 Ma.

The age models for Cores 2A and 3A reveal that accretion rates in the oldest parts of the core sustained 57–69 cm/kyr from 2.24–2.09 Ma, decreased rapidly thereafter, ultimately to <10 cm/kyr with accumulation of the Ndutu Beds. The abrupt decrease in rates in the early record of Core 2A may speculatively reflect volcanotectonic deformation associated with the buildup and climactic eruptions of the nearby Ngorongoro Volcano in the Ngorongoro Volcanic Highlands. Downward extrapolation of measured accumulation rates to depth to basement determined by seismic studies suggests an age ~ 2.5 Ma for the oldest Olduvai Beds strata in this area.

Supplementary data to this article can be found online at https://doi.org/10.1016/j.palaeo.2020.109990.

Declaration of Competing Interest

None.

Acknowledgments

We are grateful to the Tanzanian institutions that permitted and cooperated with OGCP's research, including the Tanzanian Commission for Science and Technology (COSTECH), the Tanzanian Department of Antiquities, and the Ngorongoro Conservation Area Authority (NCAA). Funding for this research was provided to the Stone Age Institute from the Kaman Foundation, the Gordon and Ann Getty Foundation, the John Templeton Foundation, the Fred Maytag Foundation, and Kay and Frank Woods, and to JKN and LJM from the National Science Foundation (BCS 1623873). $^{40}Ar/^{39}Ar$ geochronological research at the Berkeley Geochronology Center on issues of archaeometric relevance was supported by National Science Foundation grant EAR 1322017. We thank the Stone Age Institute and Indiana University Bloomington for logistical support, and we are also grateful to the late Jesuit Temba, and the entire OGCP field crew. Anders Noren, Kristina Brady, and the

University of Minnesota LacCore facility http://lrc.geo.umn.edu/laccore/ were instrumental in the logging and sampling of the cores.

References

Arculus, R.J., Ishizuka, O., Bogus, K., and the Expedition 351 Scientists, 2015. Proceedings of the International Ocean Discovery Program 351. doi:10.14379/iodp.proc.351.102.2015.

Bada, J.L., 1985. Amino acid racemization dating of fossil bones. Annu. Rev. Earth Planet. Sci. 13 (1), 241–268.

Blaauw, M., Christen, J.A., 2011. Flexible paleoclimate age-depth models using an autoregressive gamma process. Bayesian Anal. 6, 457–474.

Blumenschine, R.J., Peters, C.R., Masao, F.T., Clarke, R.J., Deino, A.L., Hay, R.L., Swisher, C.C., Stanistreet, I.G., Ashley, G.M., McHenry, L.J., Sikes, N.E., van der Merwe, N.J., Tactikos, J.C., Cushing, A.E., Deocampo, D.M., Njau, J.K., Ebert, J.I., 2003. Late Pliocene *Homo* and hominid land use from western Olduvai Gorge, Tanzania. Science 299 (5610), 1217–1221.

Curtis, G.H., Hay, R.L., 1972. Further geological studies and potassium argon dating at Olduvai Gorge and Ngorongoro Crater. In: Bishop, W.W., Miller, J.A. (Eds.), Calibration of Hominoid Evolution. Scottish Academic Press, pp. 289–301.

Deino, A.L., 2012. Ar-40/Ar-39 dating of Bed I, Olduvai Gorge, Tanzania, and the chronology of early Pleistocene climate change. J. Hum. Evol. 63 (2), 251–273.

Deino, A.L., Harrison, T., 2011. Ar-40/Ar-39 Dating of Laetoli, Tanzania. In: Harrison, T. (Ed.), Paleontology and Geology of Laetoli: Human Evolution in Context: Volume 1: Geology, Geochronology, Paleoecology and Paleoenvironment. Springer Science and Business Media, pp. 77–97.

Deino, A.L., Kingston, J.D., Glen, J.M., Edgar, R.K., Hill, A., 2006. Precessional forcing of lacustrine sedimentation in the late Cenozoic Chemeron Basin, Central Kenya Rift, and calibration of the Gauss/Matuyama boundary. Earth Planet. Sci. Lett. 247 (1–2), 41–60.

Deino, A.L., Behrensmeyer, A.K., Brooks, A.S., Yellen, J.E., Sharp, W.D., Potts, R., 2018. Chronology of the Acheulean to Middle Stone Age transition in eastern Africa. Science 360 (6384), 95–98.

Deino, A.L., Dommain, R., Keller, C.B., Potts, R., Behrensmeyer, A.K., Beverly, E.J., King, J., Heil, C.W., Stockhecke, M., Brown, E.T., Moerman, J., deMenocal, P., 2019a. Chronostratigraphic model of a high-resolution drill core record of the past million years from the Koora Basin, south Kenya Rift: Overcoming the difficulties of variable sedimentation rate and hiatuses. Quat. Sci. Rev. 215 (74), 213–231.

Deino, A.L., Sier, M.J., Garello, D., Keller, B., Kingston, J., Scott, J., Dupont-Nivet, G., Cohen, A., 2019b. Chronostratigraphy of the Baringo-Tugen-Barsemoi (HSPDP-BTB13-1A) Core – $^{40}Ar/^{39}Ar$ dating, magnetostratigraphy, tephrostratigraphy, sequence stratigraphy and Bayesian age modeling. In: A high resolution, multi-proxy record of Pliocene hominin environments in the Kenya Rift Valley: Analysis of the Baringo-Tugen-Barsemoi (BTB) Drill Core. https://doi.org/10.1016/j.palaeo.2019.109519.

Diez-Martin, F., Yustos, P.S., Uribelarrea, D., Baquedano, E., Mark, D.F., Mabulla, A., Fraile, C., Duque, J., Diaz, I., Perez-Gonzalez, A., 2015. The origin of the Acheulean: the 1.7 million-year-old site of FLK West, Olduvai Gorge (Tanzania). Sci. Rep. 5 (1), 1–9.

Dominguez-Rodrigo, M., Pickering, T.R., Baquedano, E., Mabulla, A., Mark, D.F., Musiba, C., Bunn, H.T., Uribelarrea, D., Smith, V., Diez-Martin, F., 2013. First partial skeleton of a 1.34-million-year-old *Paranthropus boisei* from Bed II, Olduvai Gorge, Tanzania. PLoS One 8 (12).

Evernden, J.F., Curtis, G.H., 1965. Potassium-Argon dating of late Cenozoic rocks in East Africa and Italy. Cur. Anth. 6, 343–385.

Fleck, R.J., Sutter, J.F., Elliot, D.H., 1977. Interpretation of discordant $^{40}Ar/^{39}Ar$ age-spectra of Mesozoic tholeiites from Antarctica. Geochim. Cosmochim. Acta 41, 15–32.

Grommé, C.S., Hay, R.L., 1963. Magnetization of basalt in Bed I, Olduvai Gorge. Nature 200, 560–561.

Grommé, C.S., Hay, R.L., 1967. Geomagnetic polarity epochs: new data from Olduvai Gorge. Earth Planet. Sci. Lett. 2, 111–115.

Grommé, C.S., Hay, R.L., 1971. Geomagnetic polarity epochs: age and duration of the Olduvai normal polarity event. Earth Planet. Sci. Lett. 10 (2), 179–185.

Grommé, C.S., Reilley, T.A., Mussett, A.E., Hay, R.L., 1970. Paleomagnetism and potassium–argon ages of volcanic rocks of Ngorongoro Caldera, Tanzania. Geophys. J. Int. 22, 101–115.

Habermann, J.M., McHenry, L.J., Stollhofen, H., Tolosana-Delgado, R., Stanistreet, I.G., Deino, A.L., 2016. Discrimination, correlation, and provenance of Bed I tephrostratigraphic markers, Olduvai Gorge, Tanzania, based on multivariate analyses of phenocryst compositions. Sediment. Geol. 339, 115–133.

Hay, R.L., 1976. Geology of the Olduvai Gorge: A Study of Sedimentation in a Semiarid Basin. University of California Press, Berkeley.

Hay, R.L., 1992. Potassium-argon dating of Bed I, Olduvai Gorge, 1961–1972. Quat. Int. 13, 31–36.

Hay, R.L., Kyser, T.K., 2001. Chemical sedimentology and paleoenvironmental history of Lake Olduvai, a Pliocene lake in northern Tanzania. Geol. Soc. Am. Bull. 113, 1505–1521.

IODP-MI, 2011. IODP Depth Scales Terminology version, p. 2.0. https://www.iodp.org/policies-and-guidelines/142-iodp-depth-scales-terminology-april-2011/file.

Keller, C.B., 2018. Chron.jl: A Bayesian framework for integrated eruption age and age-depth modelling. https://doi.org/10.17605/OSF.IO/TQX3F.

Kirschvink, J.L., 1980. The least-squares line and plane and the analysis of palaeomagnetic data. Geophys. J. Int. 62 (3), 699–718.

Kuiper, K.F., Deino, A., Hilgen, F.J., Krijgsman, W., Renne, P.R., Wijbrans, J.R., 2008. Synchronizing rock clocks of Earth history. Science 320 (5875), 500–504.

Laj, C., Channell, J.E.T., 2007. Geomagnetic excursions. In: Kono, M. (Ed.), Treatise on Geophysics. V. 5 (Geomagnetism).

Lee, J.-Y., Marti, K., Severinghaus, J.P., Kawamura, K., Yoo, H.-S., Lee, J.B., Kim, J.S., 2006. A redetermination of the isotopic abundances of atmospheric Ar. Geochim. Cosmochim. Acta 70, 4507–4512.

Lu, K., Hanafy, S., Stanistreet, I., Njau, J., Schick, K., Toth, N., Stollhofen, H., Schuster, G., 2019. Seismic imaging of the Olduvai Basin. Tanzania. Palaeogeogr. Palaeoclimatol. Palaeoecol. 533, 109246.

Manega, P.C., 1994. Geochronology, geochemistry and isotopic study of the Plio-Pleistocene hominid sites and the Ngorongoro Volcanic Highland in northern Tanzania. PhD thesis. University of Colorado, Boulder.

McHenry, L.J., 2005. Phenocryst composition as a tool for correlating fresh and altered tephra, Bed I, Olduvai Gorge, Tanzania. Stratigraphy 2, 101–115.

McHenry, L.J., 2012. A revised stratigraphic framework for Olduvai Gorge Bed I based on tuff geochemistry. J. Hum. Evol. 63 (2), 284–299.

McHenry, L.J., Deino, A.L., 2020. Geochronology and geochemistry of the Naibadad Beds, Laetoli, Tanzania.

McHenry, L.J., Stanistreet, I.G., 2018. Tephrochronology of Bed II, Olduvai Gorge, Tanzania, and placement of the Oldowan–Acheulean transition. J. Hum. Evol. 120, 7–18.

McHenry, L.J., Mollel, G.F., Swisher, C.C.I.I.I., 2008. Compositional and textural correlations between Olduvai Gorge Bed I tephra and volcanic sources in the Ngorongoro Volcanic Highlands. Tanzania. Quat. Int. 178, 306–319.

McHenry, L.J., Njau, J.K., de la Torre, I., Pante, M.C., 2016. Geochemical "fingerprints" for Olduvai Gorge Bed II tuffs and implications for the Oldowan–Acheulean transition. Quat. Res. 85 (1), 147–158.

McHenry, L.J., Stanistreet, I.G., Stollhofen, H., Njau, J., Toth, N., Schick, K., 2020. Tuff fingerprinting and correlations between OGCP cores and outcrops for pre-Bed I and Beds I/II at Olduvai Gorge, Tanzania. Palaeogeography, Palaeoclimatology, Palaeoecology 548. https://doi.org/10.1016/j.palaeo.2020.109630.

Min, K.W., Mundil, R., Renne, P.R., Ludwig, K.R., 2000. A test for systematic errors in Ar-40/Ar-39 geochronology through comparison with U/Pb analysis of a 1.1-Ga rhyolite. Geochim. Cosmochim. Acta 64 (1), 73–98.

Niespolo, E.M., Rutte, D., Deino, A.L., Renne, P.R., 2017. Intercalibration and age of the Alder Creek sanidine Ar-40/Ar-39 standard. Quat. Geochronol. 39, 205–213.

Owen, R.B., Renaut, R.W., Muiruri, V.M., Rabideaux, N.M., Lowenstein, T.L., McNulty, E. P., Leet, K., Deocampo, D., Luo, S., Deino, A.L., Cohen, A., Sier, M.J., Campisano, C., Shen, C.-C., Billingsley, A., Mbuthia, A., Stockhecke, M., 2019. Quaternary history of the Lake Magadi Basin, southern Kenya Rift: Tectonic and climatic controls. Palaeogeogr. Palaeoclimatol. Palaeoecol. 518, 97–118.

Ramsey, C.B., 2008. Deposition models for chronological records. Quat. Sci. Rev. 27, 42–60.

Reck, H., 1914. Erste vorlaufige Mitteilung über den Fund eines fossilen Menschenskelets aus Zentralafrika. Sitzungsberichten der Gesellschaft naturforschender Freunde 3, 81–95.

Reck, H., 1951. A preliminary survey of the tectonics and stratigraphy of Olduvai. In: Leakey, L.S.B. (Ed.), Olduvai Gorge. Cambridge University Press, London, pp. 5–19.

Sagnotti, L., 2013. Demagnetization Analysis in Excel (DAIE). An open source workbook in Excel for viewing and analyzing demagnetization data from paleomagnetic discrete samples and u-channels. Ann. Geophys. 56 (1).

Simon, Q., Bourles, D.L., Thouveny, N., Horng, C.-S., Valet, J.-P., Bassinot, F., Choy, S., 2018. Cosmogenic signature of geomagnetic reversals and excursions from the Reunion event to the Matuyama–Brunhes transition (0.7–2.14 Ma interval). Earth Planet. Sci. Lett. 482, 510–524.

Singer, B.S., 2014. A Quaternary geomagnetic instability time scale. Quat. Geochronol. 21, 29–52.

Stanistreet, I.G., McHenry, L.J., Stollhofen, H., de la Torre, I., 2018. Bed II Sequence Stratigraphic context of EF-HR and HWK EE archaeological sites, and the Oldowan/Acheulean succession at Olduvai Gorge, Tanzania. J. Hum. Evol. 120, 19–31.

Stanistreet, I.G., Stollhofen, H., Deino, A., McHenry, L., Toth, N., Schick, K., Njau, J., 2020a. New Olduvai Basin stratigraphy and stratigraphic concepts revealed by OGCP cores into the Palaeolake Olduvai depocentre, Tanzania. Palaeogeogr. Palaeoclimatol. Palaeoecol. 554 https://doi.org/10.1016/j.palaeo.2020.109751.

Stanistreet, I.G., Boyle, J.F., Stollhofen, H., Deocampo, D., Deino, A., McHenry, L., Toth, N., Schick, K., Njau, J., 2020b. Palaeosalinity and palaeoclimatic geochemical (elements Ti, Mg, Al) proxies vary with Milankovitch cyclicity, Beds I and II in OGCP cores, Palaeolake Olduvai, Tanzania. Palaeogeogr. Palaeoclimatol. Palaeoecol. 546 https://doi.org/10.1016/j.palaeo.2020.109656.

Stanistreet, I.G., Doyle, C., Hughes, T., Rushworth, E.R., Stollhofen, H., Toth, N., Schick, K., Njau, J., 2020c. Changing depocentre environments of Palaeolake Olduvai and carbonates as marker horizons for hiatuses and lake-level extremes (Palaeogeogr. Palaeoclimatol. Palaeoecol. This volume).

Stollhofen, H., Stanistreet, I.G., 2012. Plio-Pleistocene synsedimentary fault compartments, foundation for the eastern Olduvai Basin paleoenvironmental mosaic, Tanzania. J. Hum. Evol. 63 (2), 309–327.
Stollhofen, H., Stanistreet, I.G., McHenry, L.J., Mollel, G.F., Blumenschine, R.J., Masao, F.T., 2008. Fingerprinting facies of the Tuff IF marker, with implications for early hominin palaeoecology, Olduvai Gorge, Tanzania. Palaeogeogr. Palaeoclimatol. Palaeoecol. 259 (4), 382–409.
Tamrat, E., Thouveny, N., Tai, M., Opdyke, N.D., 1995. Revised magnetostratigraphy of the Plio-Pleistocene sedimentary sequence of the Olduvai Formation (Tanzania). Palaeogeogr. Palaeoclimatol. Palaeoecol. 114 (2–4), 273–283.
Tauxe, L., Badgley, C., 1988. Stratigraphy and remanence acquisition of a palaeomagnetic reversal in alluvial Siwalik rocks of Pakistan. Sedimentology 35 (4), 697–715.
Walter, R.C., Manega, P.C., Hay, R.L., Drake, R.E., Curtis, G.H., 1991. Laser-fusion $^{40}Ar/^{39}Ar$ dating of Bed I, Olduvai Gorge, Tanzania. Nature 354 (6349), 145–149.
Zijderveld, J.D.A., 1967. Demagnetization of rocks: analysis of results. In: Collison, P.A., Creer, K.M., Runcorn, S.K. (Eds.), Methods in Paleomagnetism. Elsevier, Amsterdam.